

RICE UNIVERSITY

**Magneto-Optical Kerr Effect and
Magnetic Circular Dichroism in
Ferromagnetic InMnAs/GaSb Heterostructures**

by

Jigang Wang

A THESIS SUBMITTED
IN PARTIAL FULFILLMENT OF THE
REQUIREMENTS FOR THE DEGREE

MASTER OF SCIENCE

APPROVED, THESIS COMMITTEE:

Junichiro Kono, Chair, Assistant Professor of
Electrical and Computer Engineering

Naomi J. Halas, Stanley C. Moore Professor of
of Electrical and Computer Engineering

Douglas Natelson, Assistant Professor of
Physics and Astronomy

Houston, Texas

April, 2002

ABSTRACT

Magneto-Optical Kerr Effect and Magnetic Circular Dichroism in Ferromagnetic InMnAs/GaSb Heterostructures

By

Jigang Wang

This thesis describes a Magneto-Optical Kerr Effect (MOKE) and Magnetic Circular Dichroism (MCD) study of ferromagnetism in III-V magnetic semiconductor heterostructures. This work was initiated due to the much recent interest in spin-related phenomena in semiconductors. The discovery of carrier/light-induced ferromagnetism in InMnAs-based heterostructures has opened up new possibilities for spin-based multifunctional devices that will integrate photonics, magnetics and microelectronics. However, an experimental demonstration of direct *ultrafast optical manipulation* of spins/magnetic order in this system has not been reported, although it is considered to be a crucial step towards *pico-* or *femto-*second operation of information encoded in the spin degree of freedom. In addition, the *origin of ferromagnetism* is still a subject of debate. To address these issues, we have developed an experimental setup for performing continuous-wave (CW) and time-resolved light-induced MOKE/MCD experiments. Our data clearly demonstrate that magnetic properties, e.g., coercivity and remanent magnetization, can be optically controlled in an ultrafast manner ($\sim ps$). The experimental results of CW and two-color time-resolved MOKE/MCD measurements are presented. Finally, the mechanism of the ultrafast MOKE response is discussed in terms of transient photo/carrier-induced modifications of exchange interaction and domain wall energy.

Acknowledgements

My desire for doing a project of spin-related phenomena in semiconductors began when I took Dr. Junichiro Kono's course after I came to Rice. I am very grateful to him for introducing me to this interesting field and also serving as my advisor for this project. I really appreciate the way he encouraged me at my work and the way he taught me how to think as a successful experimentalist. His knowledge and brilliance have influenced me deeply. I would also like to express my great thanks to Dr. Giti. A. Khodaparast, who worked with me in this project. Her enthusiasm and experience have been always an impetus for this project. I would like to express my gratitude to Dr. Naomi J. Halas and Dr. Douglas Natelson for serving on my Thesis Committee. In addition, I really enjoyed the numerous discussions with our group members. These include Dr. Marie P. Johnson, Bruce Brinson, Jun Tang, Gordana N. Ostojic, Diane C. Larrabee, and Ajit Srivastava. Special thanks go to Dr. Marie P. Johnson, who kindly proofread and gave me advice on the manuscript of my thesis. Without her help, I would not have been able to finish it in time. Finally, I would like to say that the continuous support and encouragement from my parents have allowed me to explore thus far.

List of Figures

Fig.1	Different existing theoretical models for carrier-induced ferromagnetism in III-V dilute magnetic semiconductors.	6
Fig.2	Critical temperature vs. hole concentration (left) and chemical trends for the critical temperature (right), calculated within the mean-field theory by Dietl <i>et al.</i> [11].	8
Fig.3	Energy difference between the ferromagnetic phase and antiferromagnetic phase vs. concentration of external donors, calculated within the double exchange model described in the text [9].	10
Fig.4	The density of states of the ground state InMnAs of two possible phases [9].	11
Fig.5	LCAO (linear combination of atomic orbital) calculation of electronic states of Mn impurities, nearest neighbor semiconductors sites and host semiconductor sites in (Ga,Mn)As [10].	12
Fig.6	Sketch of different responses of itinerant holes in the valence band to the movement of the collective localized spin wave.	13
Fig.7	Dispersion relations for the collective spin excitation calculated by the three theoretical models (spin-wave model, RKKY model, and mean-field model).	13
Fig.8	Comparison between the mean-field theory and a Monte Carlo simulation [20].	15
Fig.9	Different regimes of ferromagnetism in III-V magnetic semiconductors [21].	16
Fig.10	Light-induced ferromagnetic order at 5 K [12].	20
Fig.11	Electrical tuning of ferromagnetic order (22.5 K) [13].	20
Fig.12	Growth phase diagrams of (In,Mn)As on (Al,Ga)Sb (left) and on GaAs (right).	27

Fig.13	Temperature dependence of the remnant magnetization (left) and a hysteresis of Hall resistance (right) observed in a p-type InMnAs film in 1991 [4].	28
Fig.14	Polar Kerr rotation spectra of at 5.5 K for two heterostructures: 9nm(19nm)-InMnAs/136nm(195nm)-AlSb.	29
Fig.15	Polar Kerr rotation spectra at 5.5 K for different Heterostructures.	29
Fig.16	Schematic band diagram of a type-II (In,Mn)As/(Al,Ga)Sb heterostructure.	30
Fig.17	Sketch of the Clark CPA 2001+ system.	36
Fig.18	Tuning range of different operation modes of Quantronix/Light Conversion's TOPAS. First row is applicable to the OPA system in our lab.	37
Fig.19	Sketch of the Oxford Spectromag-4000-10 superconducting magnet.	39
Fig.20	Schematic diagram for the CW MCD experimental setup.	40
Fig.21	Schematic diagrams for the CW-MOKE experimental setup.	42
Fig.22	Schematic diagram for the time-resolved MOKE spectroscopy experiments.	43
Fig.23	Schematic diagram of the circuit used in the New Focus Nirvana detector feedback loop.	47
Fig.24	One cycle of quarter wave modulation using a photoelastic modulator.	48
Fig. 25	Simple sketch of idea of a Gated Integrator and Boxcar Averager.	50
Fig.26	Typical MCD hysteresis trace obtained for K22d (T = 20 K, probe laser wavelength = 780 nm).	51
Fig.27	Typical MCD hysteresis trace obtained for K285 (T = 10.6 K, probe laser wavelength = 780 nm).	53
Fig.28	MCD curve for Sample R1351 using the 780 nm laser diode at 20 K.	54
Fig.29	MCD curve for sample R1351 using the 532 nm laser at 2.2 K.	55

Fig.30	MCD signal vs. magnetic field at seven different temperatures obtained for K22d using the 780 nm laser diode.	56
Fig.31	MCD signal vs. magnetic field at seven different temperatures obtained for R1351 using the 780 nm laser diode.	58
Fig.32	The temperature dependence of the zero-field MCD signal for R1351 using the 780 nm laser diode.	59
Fig.33	MCD signal vs. magnetic field at four different temperatures obtained for sample K285 using the 780 nm laser diode.	60
Fig.34	MOKE signal vs. magnetic field for K22d. This data was taken at 30 K using the 780 nm laser diode. A Kerr rotation angle of 0.06 degree can be deduced here.	61
Fig.35	MOKE signal vs. magnetic field for K22d. This data was taken at 9.5 using a CPA with wavelength 775nm, 1 KHz repetition rate.	63
Fig.36	Two-color time-resolved pump-probe measurements of a test GaAs sample.	65
Fig.37	Two-color time-resolved MOKE measurements of K22d InMnAs heterostructure.	67
Fig.38	Two-color time resolved MOKE measurements of K22d InMnAs heterostructure. Polarization plane of CPA changed from 45 to 135 degrees.	69
Fig.39	Field sweeps at different time delay.	74
Fig.40	Temperature dependence of the hysteresis loop of sample k22d. (780 nm probe light).	77
Fig.41	Sweep rate dependence of the MCD curve for R1351 at $T = 2.170$ K.	78
Fig.42	Two-color time resolved MOKE measurements of K22d InMnAs heterostructure. “Double peak” appears inside the main structure.	79

List of abbreviations

CPA	Chirped pulse amplifier
CW	Continuous wave
DMS	Dilute magnetic semiconductor
FET	Field effect transistor
FIR	Far-infrared
LED	Light emitting diode
MBE	Molecular beam epitaxy
MCD	Magnetic Circular Dichroism
MIR	Mid-infrared
MOCVD	Metal organic chemical vapor deposition
MOKE	Magneto Optical Kerr Effect
MS	Magnetic Semiconductor
NIR	Near-infrared
OPA	Optical parametric amplifier
OVC	Outer vacuum can
PEM	Photoelastic modulator
VTI	Variable temperature insert

Table of Contents

Abstract	ii
Acknowledgements	iii
List of Figures	vi
List of abbreviations	vii
Chapter 1 Introduction	
Chapter 2 Literature Review: Semiconductor Spintronics	4
2-1. Theoretical	5
2-2. Experimental	16
Chapter 3 Magneto-Optical Kerr Effect (MOKE) and Magnetic Circular Dichroism (MCD)	22
Chapter 4 InMnAs-Based Magnetic Semiconductors and Their Heterostructures	26
4-1. Growth and characterization	26
4-2. Samples studied	29
Chapter 5 Experimental Methods	32
5-1. Lasers	33
5-2. Superconducting magnet	38
5-3. Optical setups	39
5-3.1 Optical setup for CW-MCD	40
5-3.2 Optical setup for CW-MOKE	41

5-3.3 Optical setup for two-color time-resolved MOKE..	42
5-4. Detection schemes	46
5-4.1 MCD: Photoelastic modulation	46
5-4.2 MOKE: Polarization bridge	47
5-5. Data acquisition methods	48
5-5.1 Acquisition with a lock-in amplifier	48
5-5.2 Acquisition with a Box-car integrator/averager	49
Chapter 6 Results and Discussion	51
6-1. CW MCD	51
6-2. Temperature dependence of MCD	56
6-3. CW MOKE	61
6-4. MOKE with femtosecond laser pulses	63
6-5. Two-color pump-probe measurements of GaAs	65
6-6. Two-color time-resolved MOKE	67
6-7. Measurements of nonequilibrium ferromagnetism	72
6-8. Unanswered questions	76
Chapter 7 Conclusions	80
References	82

Abstract

This thesis provides a detailed description of a Magneto Optical Kerr Effect (MOKE) / Magnetic Circular Dichroism (MCD) study of ferromagnetism in III-V Dilute Magnetic Semiconductor (DMS) Heterostructures. This work was initiated due to the much recent interest in spin-related phenomena in semiconductors [1]. The discovery of carrier/light induced ferromagnetism in InMnAs-based magnetic semiconductor heterostructures has opened up new possibilities for spin-based multifunctional devices that will integrate photonics, magnetics and microelectronics [2-5]. However, the *origin of ferromagnetism* is a still subject of debate [6-10]. The experimental demonstration of direct *ultrafast optical manipulation* of spins/magnetic order in this system, which is one of crucial steps towards *pico-* or *femto*-second operation of information encoded in the spin degree of freedom, has not been done yet. To address the above issues, we have developed an experimental apparatus for performing continuous wave (CW) and time-resolved light-induced MOKE/MCD experiments. Our data clearly demonstrate that magnetic properties, e.g., coercivity and remnant magnetization, can be controlled in an ultrafast manner ($\sim ps$). The experimental results of CW and two-color time-resolved MOKE/MCD measurements are presented. And the mechanism of the ultrafast response in terms of carrier-induced changes in exchange interaction and domain wall energy is discussed.

Chapter 1 Introduction

The spin degree of freedom, quantum nature of electrons, was totally ignored in the development of conventional charge-based microelectronics. New device concepts are being sought that employ the spin degree of freedom of electrons in addition to, or in place of, the charge (or orbital) degree of freedom of electrons. Some “spintronic” devices, like GMR read head, have brought the first round of market impact to the information storage industry.

Although the early approach to spintronics is more concentrated on the spin dependent process in metallic systems, including various metallic multilayers showing giant magnetoresistance (GMR) effect, ferromagnetic tunnel junction exhibiting tunnel magnetoresistance, and so on []. Until very recently, there has been much interest in spin-related phenomena in semiconductors [1]. This partially due to the reason that integration the “spintronic” device with the conventional semiconductor device will open up the possibility of integrating information storage and processing capabilities into a single device.

Researchers in semiconductor spintronics field are trying to make various types of innovative magnetic semiconductor heterostructures to engineer the spin, a quantum mechanical property, of electrons as well as the charge of electrons in the quantum confined structures. These ‘spintronic’ devices will enhance and expand the functionalities of existing semiconductor electronic devices and even make it possible to perform quantum computation in semiconductors using spin coherence [10].

On the one hand, in order to achieve these fascinating goals, one must first have a semiconductor material system into which spin can be easily incorporated. InMnAs films [2,3] and their heterostructures with (Al,Ga)Sb [4], the first III-V dilute magnetic semiconductor (DMS), serve as a prototype for implementing the concept of spintronics into semiconductors. The discovery of ferromagnetism in this III-V DMS system [3,4] and in GaMnAs [11] has great promise for integrating information storage and processing capabilities into a single device. Recent experiments have demonstrated the feasibility of external control of ferromagnetism in this system optically [12] and electrically [13]. Optically induced ferromagnetism in InMnAs-based magnetic semiconductor heterostructures [12] is extremely interesting in terms of opening up new possibilities for spin-based multifunctional devices that will integrate photonics, magnetics and microelectronics. Basically speaking this is a persistent photoconductivity effect and needs very long build-up time (~ 30 minutes in the experiment described in [12]), thus it is less possible towards the practical application. So a next important step is a demonstration of direct *ultrafast* optical manipulation of spins/magnetic order in this system, which can be used for *pico*- or *femto*-second operation of information encoded in the spin degree of freedom. Successful experimental demonstration of this phenomenon will be expected to intrigue great interests not only in the community of pure science, but also the community of applied science.

On the other hand, from theoretical viewpoints, we need to understand this spin degree of freedom in these magnetic semiconductor heterostructures in order to explore the potential and design principle for such high-performance spin-based device. However, the origin of ferromagnetism, which is apparently induced by free holes, is still a subject of

intense debate. Various models have been proposed, including a mean-field model, a double-exchange model, a Ruderman-Kittel-Kasuya-Yoshida (RKKY) model, a spin wave model, ... etc. [5-9]. However, currently, there is no single theory that can accurately predict Curie temperatures for different III-V DMSs in different carrier density regimes. Also, many issues still remain controversial. One of the important open questions is whether the carriers responsible for ferromagnetic order are *p*-like or *d*-like, that is, originate from the valence band or the impurity band or some sort of mixture of the two. Several recent experiments have shone new light on this problem []. But still some new experimental data are urgent needed to permit a better understanding of the carrier-induced ferromagnetism.

In this project, we are performing CW and time-resolved magneto-optical Kerr effect (MOKE) / magnetic circular dichroism (MCD) experiments to answer the above questions. We have studied several InMnAs-based samples and results will be discussed in detail. I should point out here that the two-color time-resolved MOKE spectroscopy in InMnAs-based DMS heterostructures we proposed here is a powerful tool to study *picosecond*, temperature dependent spin dynamics and carrier-induced nonequilibrium ferromagnetism. The two-color time-resolved MOKE experiments by ultrafast optical pumping will identify the process(es) governing the spin coherence of excited photo-carriers and the loss of their coherence in semiconductors, which is of utmost current interest in the community in order to achieve ultrafast semiconductor spintronics.

This report is organized as follows: Chapter 2 will review the background knowledge and literature in this field. Our method to probe ferromagnetism in III-V DMSs, i.e., MOKE/MCD spectroscopy, will be discussed in Chapter 3. Chapter 4 will

concentrate on the features of the material system of III-V DMSs. In Chapter 5, a detailed description and discussion of the experimental design will be presented. Results and discussion of CW-MOKE/MCD and two-color time resolved experiments will be given in Chapter 6. Finally, conclusions and summary will be presented.

Chapter 2 Background and literature review

Studies of spin-dependent transport, the first area of interest in the field of spintronics, actually emerged from research on spin behaviors in metal-based devices. Owing to the discovery of the Giant Magneto-Resistance (GMR) effect, metal-based spintronics is already being used in state-of-the-art computer hard drives [14]. The physical model of “spintronic” devices like magnetic random access memory (MRAM) was proposed a long time ago and the real products will be released to the market in the very near future. Spintronics is now becoming increasingly centered on semiconductor materials and fabrication techniques, partially due to the desire to integrate spintronic devices with conventional microelectronics devices [1]. Many proposed or already existing devices based on semiconductor spintronics have stimulated intense interests in both the pure science and applied science communities. These devices include spin FETs, ferromagnetic FETs, spin LEDs, spin RTDs, spin optical switches working at terahertz frequencies, ... etc. [1,13,15,16]. It is believed that, by combining the current photonics and microelectronics with magnetic cooperative long-range order, one will be able to create “multifunctional” devices, which could not be realized separately.

However, major challenges exist in many places. In this Chapter I will give a review of the field on both the experimental side and the theoretical side, placing our research project in the right context. On the theoretical side, our main interest is to understand one of the most fundamental problems in the field: *What is the origin of ferromagnetism in the III-V DMS?* Thus, in Section 2-1, I will explain the main existing theoretical models and intense controversies in the field. On the experimental side, we

are trying to *ultrafast direct optical control the long-range magnetic cooperative behaviors inside III-V DMS*, in a reversible manner. Thus, in Section 2-2, I will review the field of semiconductor spintronics in the experimental side by placing the concentration on the recent progress of external control of ferromagnetism in III-V DMS achieved to date.

Section 2-1 Review from the theoretical side

In this section, I will explain the main ideas behind the existing theoretical models in the field and compare the results of theoretical simulations from these different models.

Figure 1 summarizes the different models I am going to discuss [5-9].

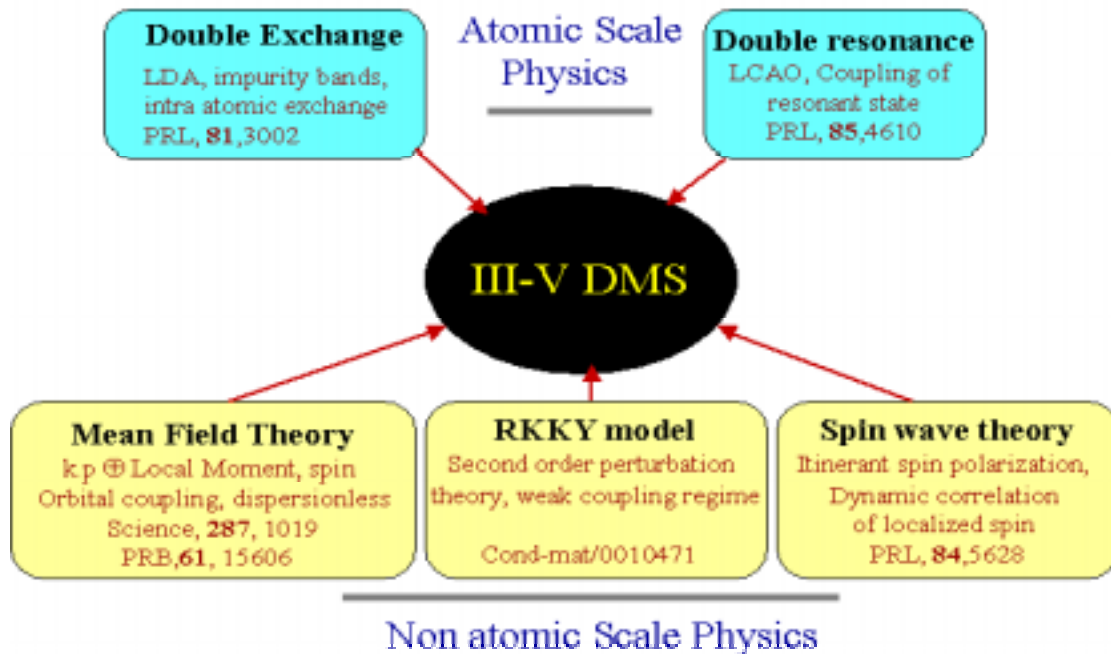


Fig. 1 Different existing theoretical models for carrier-induced ferromagnetism in III-V dilute magnetic semiconductors [5-9].

The typical Hamiltonian including kinetic-exchange interaction is expressed as

$$H = H_m + H_L + \sum_{I,j=v} J_{pd} \delta(\vec{r}_j - \vec{R}_I) \vec{s}_j \cdot \vec{S}_I, \quad \dots (1)$$

where H_m is the Hamiltonian of the magnetic ions, H_L is for the carriers in the valence bands, which are normally described by a four- or six-band Luttinger Hamiltonian depending on the Fermi energy and the spin-orbit coupling strength inside the valence bands. Different theoretical models have been proposed to solve this Hamiltonian to get the right physics and magnetic properties of this many-body system. I will describe the physical picture of these models below:

- Mean-field model [7]:

A mean field model can be obtained in the approach by taking the Ising limit of the exchange coupling term, i.e., replacing $\vec{s}_j \cdot \vec{S}_I$ by $S_z s_z$. The effective fields felt by the valence band holes and the local spins are

$$\vec{h} = JN\hat{\Omega}\langle M \rangle, \quad \vec{H} = J\vec{s}(\vec{r}), \quad \dots(2)$$

respectively. Also, one needs to make the following replacement (the virtual crystal approximation):

$$\sum_I \delta(\vec{r}_j - \vec{R}_I) \rightarrow N_{Mn} \quad \dots (3)$$

Using a six-band $\mathbf{k}\cdot\mathbf{p}$ theory for the free holes plus the Hamiltonian of the local spins, one can get the free energy of the whole system. By minimizing this free energy, one can get the critical temperature predicted by the mean field model [7], i.e.,

$$T_c^{MF} = \frac{\chi_p}{(g^* \mu_b / 2)^2} \frac{S(S+1)NJ_{pd}^2}{12} \quad \dots (4)$$

Different valance band parameters and hole concentrations in the concrete material system result in different χ_p , the Pauli susceptibility of free carriers. In a simple parabolic-band model, assuming strongly degenerate holes as well as the absence of spin-orbit interaction, one can get

$$\chi_p \propto \mu_B * g(\epsilon_F), \quad g(\epsilon_F) = M_{dos}^* k_f / \pi^2 \hbar^2 \quad \dots (5).$$

From Eqs. (4) and (5) we can conclude, within the mean-field theory, that one can increase T_c either by narrowing the free carrier band(s) or placing its Fermi energy at a density-of-states peak. Also, from Eqs. (4) and (5) one can see that the mean field T_c is proportional to $n^{1/3} * N_{Mn}$. The hole-density dependence of the critical temperature as well as the chemical trends of different materials for a fixed hole density ($3.5 \times 10^{20} \text{ cm}^{-3}$) and Mn concentration (5%) was calculated by Dietl *et al.* within the mean-field model [7] and the main results are shown in Fig. 2 below.

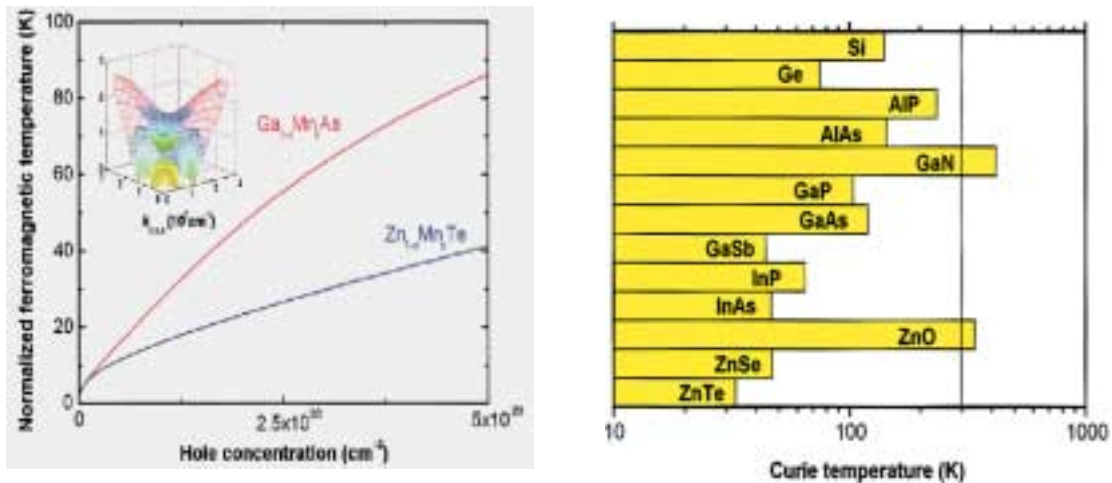


Fig. 2 Critical temperature vs. hole concentration (left) and chemical trends for the critical temperature (right), calculated within the mean-field theory by Dietl *et al.* [7].

As can be seen in Fig. 2 this work predicted the possibility of room temperature ferromagnetism in GaN and ZnO. Many groups are currently pursuing this possibility.

Within the mean-field picture, the spin splitting gap (at zero external magnetic field H) for the free carriers is $N_{\text{Mn}}J_{\text{pd}}S$, and the energy gap for an impurity-spin excitation is $J_{\text{pd}}P/2$, where P is the net spin polarization of the free carriers defined as $P = p_{\text{up}} - p_{\text{down}}$. This leads to a single dispersionless low-temperature excitation energy, which is definitely not true in reality. The collective excitation energy of a localized spin wave is always smaller than this mean-field energy gap. The mean-field picture neglects the correlations between the local-moment spins and the free-carrier states and, therefore, fails to describe the existence of low-energy long-wavelength spin excitations. This collective excitation can destroy the ferromagnetic phase at finite temperature and make the ferromagnetic phase unstable.

- The RKKY model [8,17]:

The RKKY theory is a second-order perturbation theory, which means that the exchange coupling to the holes only gives them a small effect compared to the kinetic energy. The RKKY exchange Hamiltonian between the localized spins at sites i and j is expressed as $H = -J_{ij}S_i^*S_j$, where J_{ij} can be calculated by the second order perturbation theory and is given below [8]:

$$J_{ij} = -\frac{2mk_F^4}{\pi\hbar^2} J_{pd}^2 F(2k_F r_{ij}) \exp\left(-\frac{r_{ij}}{l}\right). \quad \dots (6)$$

Here $F(2k_F r_{ij})$ is the quantum oscillation term and l is the mean free path of the free carriers. Using Eq. (6) one can get the critical temperature T_c

$$T_c = \frac{1}{3} xS(S+1) \sum z_r J_{ij}(r), \quad \dots (7)$$

where Z_r is the r_{th} nearest group-III sites.

The traditional RKKY picture provides an excellent description of long-range magnetic interaction in dilute systems and has succeeded in explaining the hole induced ferromagnetism discovered in a IV-VI compound PbSnMnTe [17]. In addition, T_c , calculated within the RKKY model for different metallic samples of (Ga,Mn)As, is in excellent agreement with the existing experimental data [8]. However, there are problems with using the RKKY picture in the III-V DMS case. These problems include: 1) RKKY model needs the perturbation smaller than the kinetic energy of holes. That is to say, the exchange coupling J_{pd} (for instance, around 1 eV in GaMnAs and around 0.7 eV in InMnAs) should be smaller than the Fermi energy (around 300 meV in GaMnAs) [8]. This condition is clearly not met in reality. 2) If the carriers in such systems originate from the Mn d states (impurity band), which are far from free-electron-like, the RKKY picture may not even be a realistic starting point [5].

- Double exchange model [5]:

Opposite to the RKKY model, the double exchange model starts from the d -band formed by transition metal impurities. Based on the local density approximation (LDA) and the coherent potential approximation (CPA) combined with the *ab initio* Korringa-Kohn-Rostoker method, the double exchange model calculates the ground state of the (In,Mn)As DMS system. The physical picture here is that, when the exchange-coupling width is greater than the bandwidth and the carriers are nearly half filling the density of states, an increase in the carrier density will stabilize the ferromagnetic phase instead of the antiferromagnetic phase. This energy gain is proportional to the carrier concentration. Therefore, the compensation of holes by external donors will destabilize the

ferromagnetic state (Fig. 3) [5]. Also, this model shows an interesting result: the ground state of InMnAs is half metallic (Fig. 4) [5].

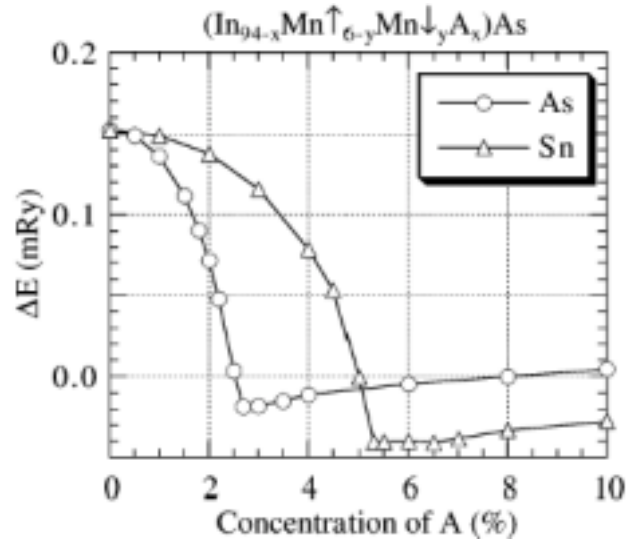


Fig. 3 Energy difference between the ferromagnetic phase and antiferromagnetic phase vs. concentration of external donors, calculated within the double exchange model described in the text [5]. It can be seen that donors destabilize the ferromagnetic phase with respect to the anti-ferromagnetic phase.

- Double resonance model [6]:

In order to solve the obvious contradictions between the RKKY and double exchange models, another theoretical model was proposed [6]. This model, a double resonance model, attempts to take an intermediate approach between the two models. By using linear combination of atomic orbital (LCAO) calculations, this study shows that Mn impurities introduce resonant states at the top of the down spin valence band (peak A in Fig. 5). This “double resonance” mechanism gives a strong and long-ranged ferromagnetic coupling between Mn moments and stabilizes the ferromagnetic phase both in the metallic side and the insulating side. The large values of the coupling

constant estimated in the RKKY model can be interpreted by the enhancement of the density of states due to the resonant state near E_F [6].

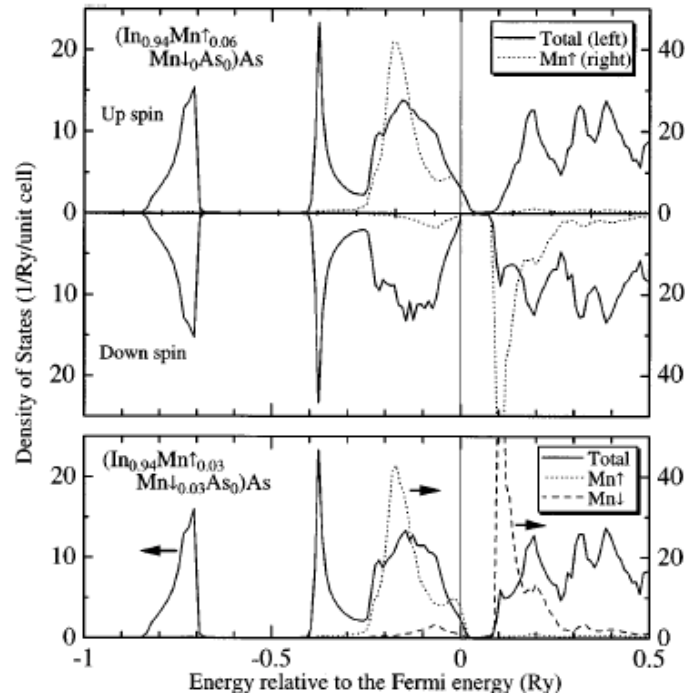


Fig. 4 The density of states of the ground state InMnAs of two possible phases. Half-metallic nature appears in the results [5]. Top panel: density of states of the ferromagnetic phase; lower panel: density of states of the antiferromagnetic phase.

- Spin-wave theory [9]:

The other drawback the mean-field model and RKKY model share is that they totally neglect the arbitrary itinerant carrier polarization and dynamic correlations between localized spins. This collective excitation of localized spins can destroy the ferromagnetic phase at finite temperature. In order to incorporate

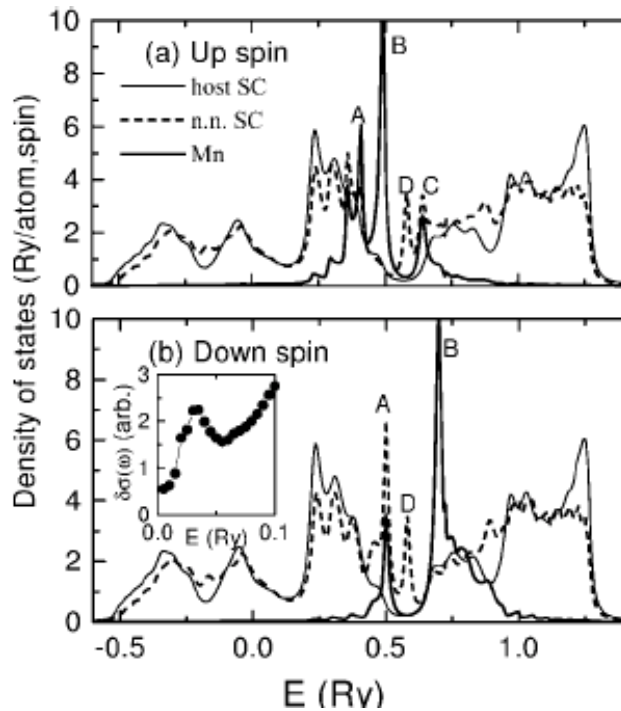


Fig. 5 LCAO (linear combination of atomic orbital) calculation of electronic states of Mn impurities, nearest neighbor semiconductor sites and host semiconductor sites in (Ga,Mn) As. Peak A of the down spin part of Mn impurities, which is located at the top of the valance band, is strongly resonant with nearest neighbor semiconductor sites density of states [6].

this part of interaction and give some specific criteria for the different regimes, a spin-wave model was proposed by König *et al.* [9,18]. Here one needs to differentiate weak coupling and strong coupling cases in the III-V DMS system. Intuitive pictures are shown in Fig. 6 below:

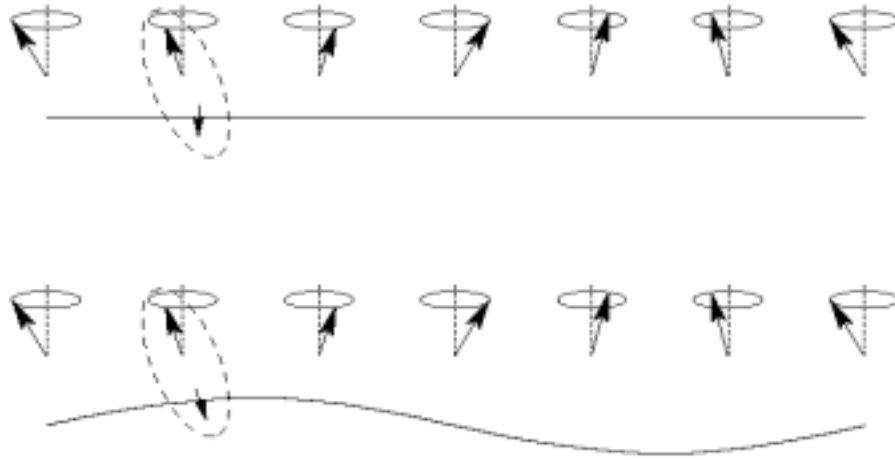


Fig. 6 Sketch of different responses of itinerant holes in the valence band to the movement of the collective localized spin wave. 1) Upper curve: the kinetic energy of carriers is minimized and the exchange energy is increased. 2) Lower curve: the exchange energy of free holes is minimized and the kinetic energy is increased [18].

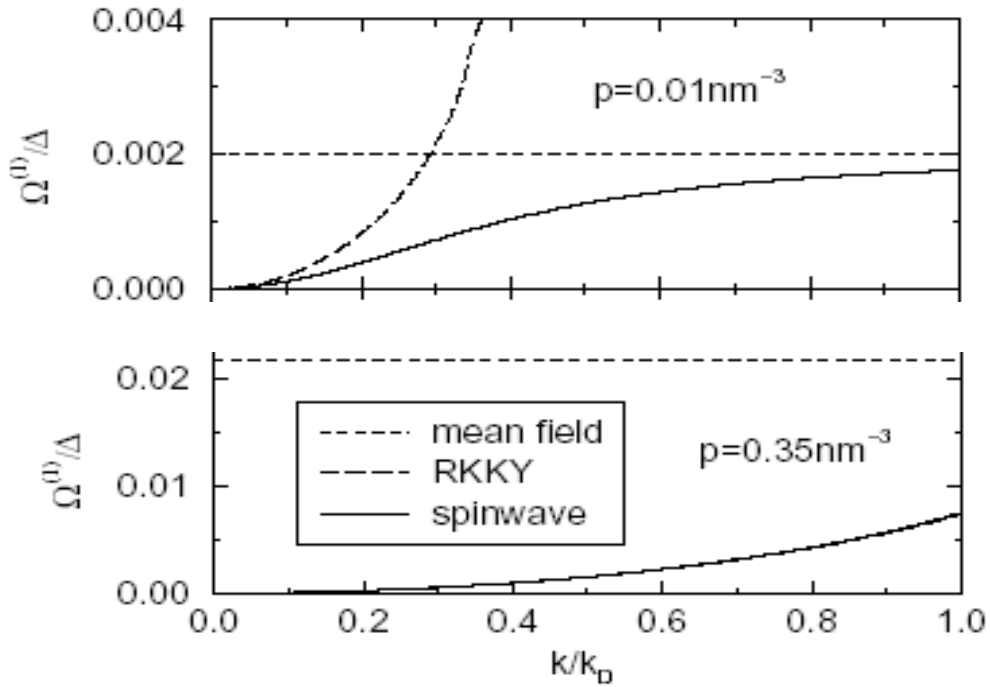


Fig. 7 Dispersion relations for the collective spin excitation calculated by the three theoretical models (spin-wave model, RKKY model, and mean-field model). The upper panel is for $\Delta/\varepsilon_F = 0.35$ (low density, weak coupling) and the lower panel is for $\Delta/\varepsilon_F = 2.79$ (high density, strong coupling) [18].

What will happen to the free holes when collective excitations of localized spins exist in these two different regimes, i.e., strong coupling $\Delta = J_{pd} N_{M_n} S > \varepsilon_F$ and weak coupling $\Delta = J_{pd} N_{M_n} S < \varepsilon_F$? In Fig. 6 the strong coupling regime is depicted in the lower figure: the holes follow the localized spin everywhere in space in order to minimize the exchange energy. The weak-coupling regime is depicted in the upper figure: the holes want to stay uniformly to minimize the kinetic energy. Therefore, the collective excitation energy is different in the above two cases. Figure 7 shows theoretical calculation results for the spin wave dispersion for different parameters corresponding to different regimes [18]. One can clearly see the different behavior of the different models in different regimes.

From the above theoretical calculations, we can conclude that the RKKY model is suitable only for the weak-coupling regime. In addition, the spin stiffness of the two cases is obviously different, and, in fact, the spin stiffness is different in the different regimes. Spin stiffness is a quantity to measure how easily one can flip spin. In other words, from this quantity, we can know how easily one can destroy the long-range spin order at finite temperature. The spin stiffness in the strong coupling limit depends differently on the exchange constant J_{pd} , the effective mass m^* and the concentration N_{Mn} from the weak coupling limit, and so we should expect different dependences of T_c on the above parameters in the different regimes. For instance, the mean-field theory becomes more inappropriate in systems with larger itinerant densities of states (see Fig. 8) [19].

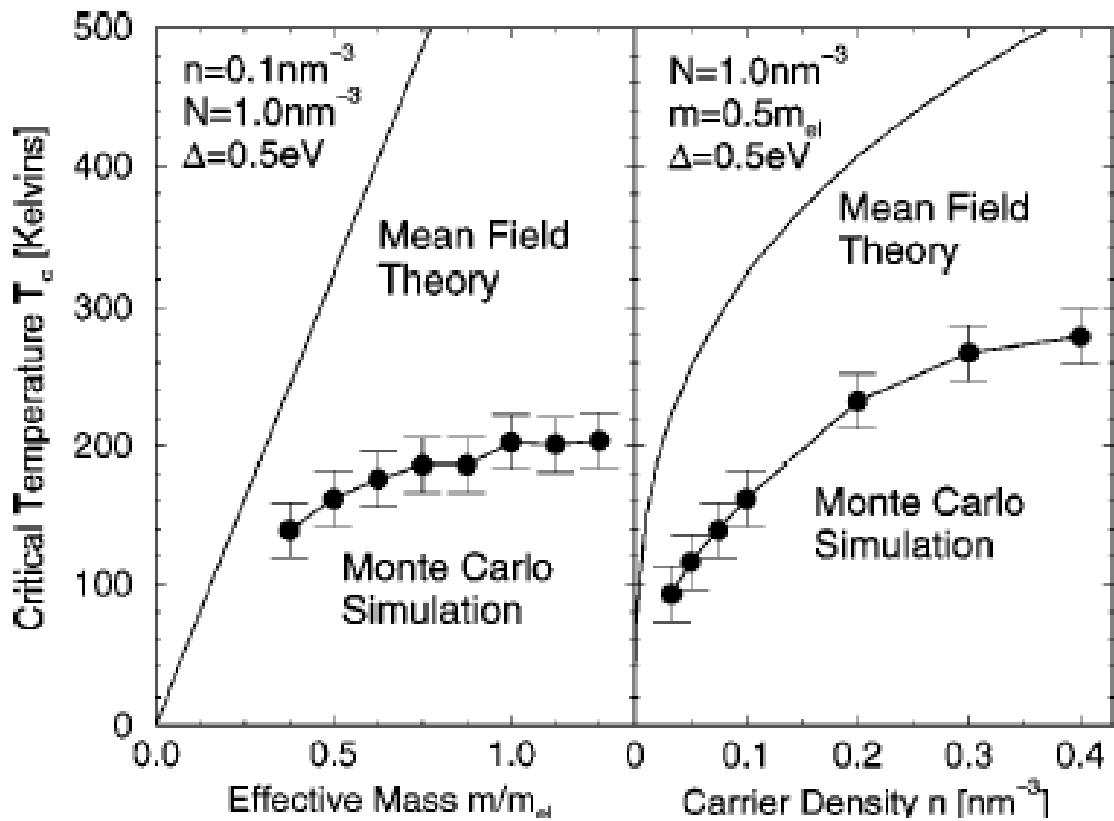


Fig. 8 Comparison between the mean-field theory and a Monte Carlo simulation [19]. Left panel: predicting T_c vs. effective mass in the regime of $n/N = 0.1$ by the two theoretical models. Mean-field model overestimates T_c , thus is an inappropriate description in this regime. Right panel: the mean-field model becomes more and more inappropriate at high carrier densities.

As a conclusion of this section, Fig. 9 shows that we need different models for addressing different physics in the different regimes [20].

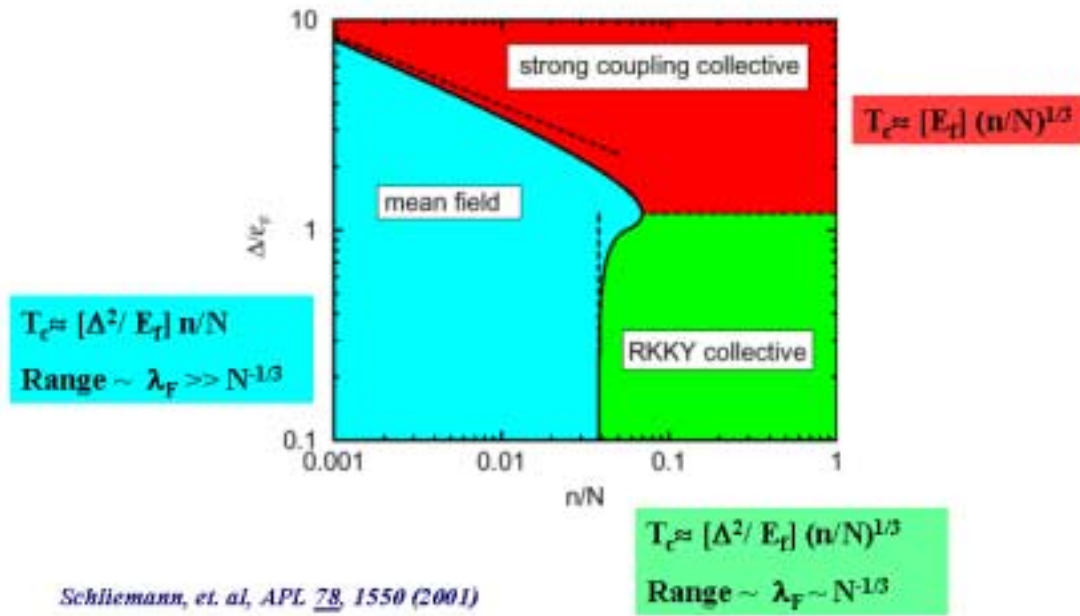


Fig. 9 Different regimes of ferromagnetism in III-V dilute magnetic semiconductors [20]. Different expressions for the critical temperature are shown for the different regimes.

Section 2-2 Review from the experimental side

Current technology in the semiconductor electronics industry has achieved a remarkable degree of material purity and technical precision. These fabrication innovations provide an opportunity to invent new materials and devices in ways that are compatible with existing electronics technology. Experimentally speaking, at a fundamental level, one needs to address and overcome five critical issues in the semiconductor spintronics research field to lead to practical use: first, how to create or inject spins in semiconductors and how to make an originally non-magnetic semiconductor become magnetic or even ferromagnetic; second, how to maintain spin coherence long enough for any useful applications; third, how to transfer spins over a long distance or even across an interface between different heterostructures without

losing their coherence; fourth, how to operate spin coherence ultrafast and efficiently; and finally, how to detect a single spin, which is essential for quantum computation using spin coherence.

Roughly speaking, current experimental efforts can be divided into these five categories and I will briefly review the current status of each of these sub-fields below:

1. Electric spin injection and electrical spin detection.

This type of experiment can be traced back to the very early spin tunneling experiments in metals by Johnson and Silsbee [21]. Ohmic spin injection from a ferromagnetic metal into a semiconductor and tunnel injection from a ferromagnetic STM tip to a semiconductor have been proposed and demonstrated to date. However, such processes have been proven to be difficult [22]. Even though much effort has been expended, 4.5% efficiency seems to be the highest reported value, using spin polarized ohmic injection from a ferromagnet into InAs around 10 K [22].

2. Electrical spin injection and optical spin detection

Instead of electrical transport measurements, the electroluminescence technique provides another effective way to detect spin polarization. Injecting spin using paramagnetic II-V DMS with an external magnetic field or using ferromagnetic III-V DMS without an external magnetic field into semiconductor quantum well have been reported [16]. In both cases, the researchers were able to inject their spin-polarized current into a GaAs-based LED structure with an efficiency of about 90 percent. Such kind spin-LED is not expected much practical use, but it is a very powerful “meter” for detecting the spin polarization experimentally.

3. Optical injection and optical detection

Femtosecond laser techniques, such as time-resolved pump-probe techniques, have been very useful for addressing a series of essential problems in the field. Spin polarized or even spin coherent carriers are created inside the normal III-V semiconductor heterostructures by an ultrafast pump pulse and a delayed probe pulse detects spin polarization locally or non-locally to answer various questions: how decoherence happens when spin moves within the same layer or across interfaces [23], and how fast one can control or operate spin coherence. A recent experiment [24] has shown that an ultrafast “tip” of electron spin coherence of normal III-V semiconductor heterostructures in the femtosecond time scale is possible. I should point out here that *ultrafast* optical manipulation of spin degree of freedom is the only way to achieve above *terahertz*, *ultrafast* semiconductor spintronics, which should be crucial for the development of quantum information and communication using spin degree of freedom in the semiconductors.

4. Optical injection and electrical detection

Recently, S. D. Ganichev *et al.* reported that a net spin polarization could be achieved in a GaAs-based quantum well by direct optical pumping [25]. The net spin polarization was then converted into a directed electrical current, where the current direction depended solely on the helicity of the pump light [25]. A phenomenological spinless theory indicates that the whole effect can be described as a second harmonic generation process due to broken symmetry. Microscopically, the reduced dimensionality of the quantum well structure lowers the symmetry of the system and therefore lifts the degeneracy of different spin energy bands in k space. Thus, unbalanced spin population due to optical pumping will result in a net electrical current. These spin-

polarized currents, perpendicular to the direction of the incident light beam, can be detected electrically. This was a demonstration of optical spin injection and electrical spin detection.

5. Magnetic doping and external control of ferromagnetic order

Doping magnetic ions into normal II-V or III-V semiconductors is the most direct way to combine the long-range cooperative order with interesting transport properties of semiconductors. Extreme useful system is III-Mn-V dilute magnetic semiconductors. As stated above, InMnAs films [2,3] and their heterostructures with (Al,Ga)Sb [4], the first III-V dilute magnetic semiconductor (DMS), serve as a prototype for implementing the concept of spintronics into semiconductors. The discovery of ferromagnetism in this III-V DMS system [3,4] and in GaMnAs [11] brings a big impact to the basic science as well as the applied science.

Recent demonstrations of externally controlling the magnetization to date are really promising for adding new functionalities to the current electronics. As I have reviewed in Section 2-1 in this chapter, the origin of ferromagnetism in III-V DMS is believed to be carrier induced. That is one of the motivations for externally controlling the ferromagnetism. One can, in principle, tune the degree of ferromagnetic order in III-V DMS by tuning the carrier concentration. Possible control of ferromagnetic order in InMnAs/GaSb heterostructures is of particular interest for our experiments. In 1997, S. Koshihara *et al.* performed a striking experiment that demonstrated the establishment of ferromagnetic order by photogenerated carriers in InMnAs/GaSb-based DMS heterostructures [12]. This was achieved by isothermally and reversibly (Fig. 10) tuning the hole density around T_c . This is a persistent photoconductivity effect, which means

the photo-generated holes, and electrons are separated at the different layers. These carriers will stay persistently and accumulate with time. So that means this effect is an irreversible process. Weak, incoherent light source are used as a pump light and surprising long build-up time (~30 minutes) was reported. Such features of the current experiment make it less usable in the practical applications, especially not applicable to the ultrafast semiconductor spintronics as mention above.

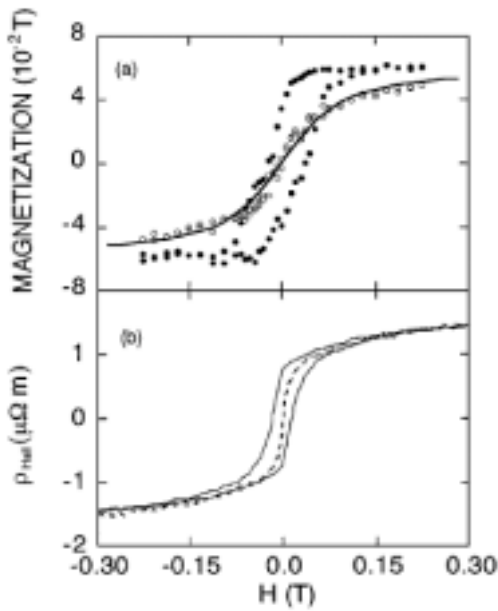


Fig10

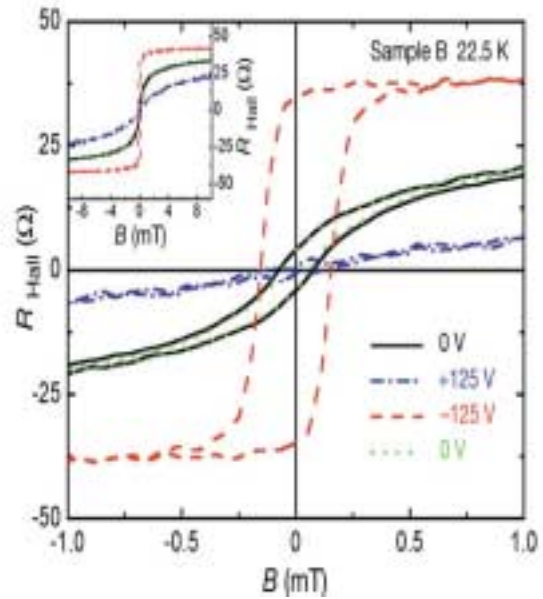


Fig 11

Fig. 10 Light-induced ferromagnetic order at 5 K [12]. **Fig. 11** Electrical tuning of ferromagnetic order (22.5 K) [13]. Anomalous Hall effect measurements are used in these studies to detect ferromagnetic order in (In,Mn)As heterostructures.

Last year H. Ohno's group in Japan varied the transition temperature of hole-induced ferromagnetism in (In,Mn)As heterostructures around 35 K (see Fig. 11) by an electrical tuning method using an FET structure [13]. Some unusual features of InMnAs-based heterostructures made it possible and much easier to control ferromagnetic order

than the other well-known III-V DMS system, (Ga,Mn)As based heterostructures. The mechanism will be explained in Chapter 4, section 2. These remarkable demonstrations are all due to long-time carrier accumulation effects within the magnetic layers.

Finally I want to point out understanding and controlling of the spin dynamics in such ferromagnetic semiconductor system is considered to lead to new class of “quantum electromagnetics [1]. Some proposals of quantum computation are based on the manipulation of spin coherence to achieve quantum logic gate operation (as an example, see [31]). We should expect that combining ultrafast optical technique and such ferromagnetic semiconductor system would lead to the new stage of semiconductor spintronics. Such kind experimental design will be presented in Chapter 5. Experimental results will be discussed in Chapter 6.

Chapter 3 Magneto-optical Kerr effect and magnetic circular dichroism

The magneto-optical Kerr effect (MOKE) / magnetic circular dichroism (MCD) is a sensitive tool for probing magnetic properties of solids. The existence of finite magnetization lowers the degree of symmetry of the system, resulting in a different microscopic response to right (RCP) and left (LCP) circularly polarized light. That is the origin of Kerr rotation and ellipticity. When a linearly polarized light beam is reflected from the surface of a ferromagnet, Kerr rotation is observed as a rotation of the polarization plane of the light. The rotation angle depends on the magnetization of the sample under study. The two circularly polarized light waves (normal modes) generally propagate with different refractive indices or different phase velocities. If the sample exhibits absorption, then the absorption coefficients for right circular and left circular polarized light are also different. Hence, when linearly polarized light is reflected from the sample surface, it becomes elliptically polarized. This effect is called circular dichroism, in general, and Magnetic Circular Dichroism, in particular, when the anisotropic indices or absorption coefficients are induced by magnetization. Generally, we can define a complex MOKE tensor, whose real part and imaginary part correspond to the Kerr rotation and MCD, respectively.

MOKE/MCD is fundamentally related to spin polarized electronic band structure. Generally speaking, a MOKE/MCD signal depends on the transition strength (dipole matrix elements and joint density of states of the coupling states), the net electron spin polarization, and the spin-orbit coupling strength (Δ_{LS}). This makes the magneto-optical

effects sensitive to the magnetic electron states, i.e., d states in the transition-metal ions. Thus, for example, the whole spectrum of polar Kerr angle vs. wavelength in InMnAs/(Al,Ga)Sb heterostructures can be related to spin-polarized electronic transitions, which can only be due to Mn $3d$ local moments [26]. The dependence of the magneto-optical effects on Δ_{LS} is a characteristic of the electronic states involved. For instance, this makes d states distinguishable from s or p states. MOKE/MCD spectra provide not only information about the joint density of states, which can be obtained by normal optical measurements, but also about the electron spin polarization of states participating in the magneto-optical transitions [28]. Therefore, the MOKE signal is sensitive to the magnetic properties of the sample under study [27].

There are different types of MOKEs, depending on the relative direction of the magnetization to the plane of incidence. Depending on whether the direction of the magnetization is parallel to the surface normal, parallel to the surface and in the plane of incidence, or parallel to the surface and perpendicular to the plane of incidence, MOKE is called the polar Kerr effect, the longitudinal Kerr effect or the transverse Kerr effect, respectively. In our case, we mostly consider the polar Kerr effect case because the easy axis of InMnAs/(Al,Ga)Sb is usually perpendicular to the sample surface as stated in the previous chapter.

We can define the dielectric constant in matrix form as

$$\boldsymbol{\varepsilon}(M, \boldsymbol{\omega}) = \begin{pmatrix} \boldsymbol{\varepsilon}_{xx} & \boldsymbol{\varepsilon}_{xy} & 0 \\ -\boldsymbol{\varepsilon}_{xy} & \boldsymbol{\varepsilon}_{xx} & 0 \\ 0 & 0 & \boldsymbol{\varepsilon}_{zz} \end{pmatrix}, \dots \quad (8)$$

where all the components in the matrix may be complex, i.e., $\epsilon_{ij} = \epsilon'_{ij} + i\epsilon''_{ij}$. Then the magneto-optical constant is defined as $Q = i\epsilon_{xy} / \epsilon_{xx}$. All the components above depend on the magnetization M (in the z direction), and the following conditions are satisfied: $\epsilon_{ij}(-\vec{M}, \omega) = \epsilon_{ji}(\vec{M}, \omega)$ (Onsager relations). Using the definitions above, the normal incidence polar MOKE angle and ellipticity can be expressed as

$$\theta_K = F_2(n, k)\epsilon'_{xy} + F_1(n, k)\epsilon''_{xy}, \quad \dots (9a)$$

$$\eta_K = F_1(n, k)\epsilon'_{xy} - F_2(n, k)\epsilon''_{xy}, \quad \dots (9b)$$

where n and k are the real and imaginary parts of the refractive index, and

$$F_1(n, k) = \frac{A}{A^2 + B^2} \quad \dots (10a)$$

$$F_2(n, k) = \frac{B}{A^2 + B^2}, \quad \dots (10b)$$

where A and B are polynomial functions of n and k and related to the diagonal elements of the dielectric constant matrix as

$$A = n(n^2 - 3k^2 - 1) \quad \dots (11a)$$

$$B = k(-k^2 + 3n^2 - 1). \quad \dots (11b)$$

Here we assume that the orientation of magnetization and light propagation is in the z direction [27].

When the sample is transparent, the basic formula for the polar Kerr effect in the case of normal incidence can be expressed as

$$\tilde{\Phi}_K = \Phi_k + i\psi_k = i\epsilon_{xy} / \sqrt{\epsilon_{xx}} (\epsilon_{xx} - 1). \quad \dots (12)$$

This formula is well known in the literature [29] and useful if the above condition is satisfied. However, under our experimental conditions, this formula is not strictly correct.

For the arbitrary incidence, the complex MOKE angle can be expressed as

$$(\theta_K^P)^{Pol} = \frac{\cos \theta_0}{\cos(\theta_1 + \theta_0)} * \left\{ i \epsilon_{xy} / \sqrt{\epsilon_{xx}} (\epsilon_{xx} - 1) \right\} \dots (13a)$$

$$(\theta_K^S)^{Pol} = \frac{\cos \theta_0}{\cos(\theta_1 - \theta_0)} * \left\{ i \epsilon_{xy} / \sqrt{\epsilon_{xx}} (\epsilon_{xx} - 1) \right\}. \dots (13b)$$

Here θ_0 and θ_1 are the incidence angle and refractive angle, respectively. In this expression, it can be seen that the second factor inside the bracket is identical to the formula for the polar Kerr effect for normal incidence in a transparent sample [29]. By measuring the rotation angle (MOKE) or ellipticity (MCD) experimentally, one can monitor the magnetization change inside the sample under study.

Chapter 4 Material system: InMnAs-based dilute magnetic semiconductors and their heterostructures

The first successful doping of Mn ions into III-V InMnAs semiconductor exceeding the heavy doping regime was reported in 1989 [2]. The subsequent discovery of ferromagnetism in p-type InMnAs films in 1991 triggered great interest in this sample system [3]. Furthermore, Curie temperatures as high as 35 K were obtained as early as 1993 by using InMnAs/(Al,Ga)Sb heterostructures instead of films [4]. The low hole concentration necessary for mediating ferromagnetic exchange interaction in this system compared with its counterpart GaMnAs system also makes it possible to control the magnetic order in the system. The unusual type-II band alignment of InMnAs/GaSb heterostructures is inherently suitable for band structure engineering [12]. In addition, a large built-in electric field can accumulate holes within the magnetic layer when optical pumping or electrical gating is used [12,13].

Next in Section 3-1, I will discuss the growth conditions and basic characteristics of InMnAs films. In Section 3-2, InMnAs/(Al,Ga)Sb heterostructures will be discussed.

Section 3-1 Growth and characterization

The major challenge in making III-V semiconductors magnetic has been surface segregations that occur when one tries to incorporate magnetic elements (such as Mn)

into the compounds beyond the heavy doping regime. Since, roughly speaking, magnetic effects are proportional to the concentration of the magnetic ions, one needs to increase the magnetic impurity density as much as possible, normally higher than 10^{18} cm^{-3} . Non equilibrium low temperature molecular beam epitaxy (MBE) was the key to the breakthrough in 1989 at IBM [2]. When the crystal is grown at low temperature by MBE, a second phase is suppressed due to the lack of energy necessary for forming the second phase but it still allows epitaxial growth of a single-crystal alloy. Figure 12 shows growth phase diagrams for InMnAs on (Ga,Al)Sb and on GaAs.

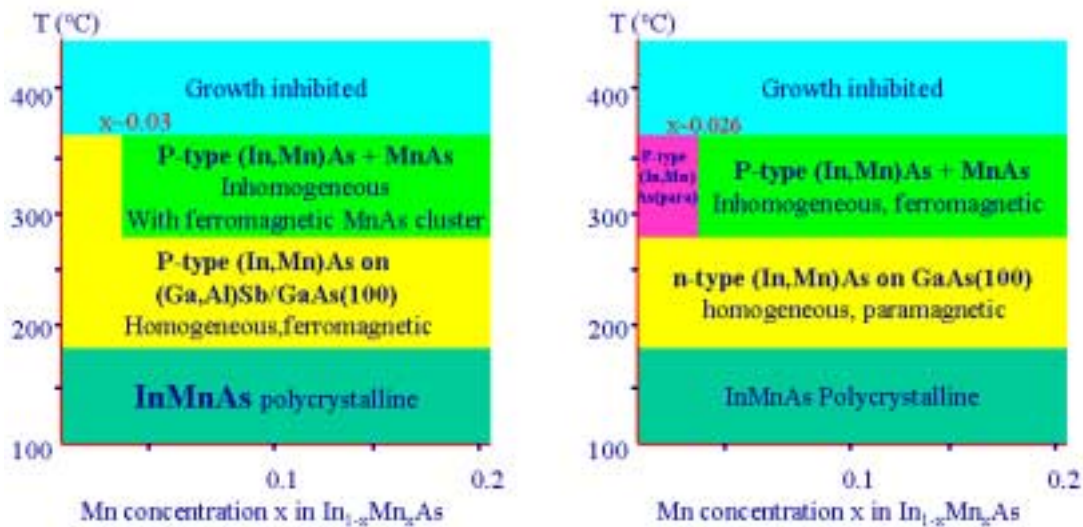


Fig. 12 Growth phase diagrams of (In,Mn)As on (Al,Ga)Sb (left) and on GaAs (right).

The subsequent discovery of ferromagnetism in p-type InMnAs films in 1991 [3] made one of the milestones in the field (see Fig. 13).

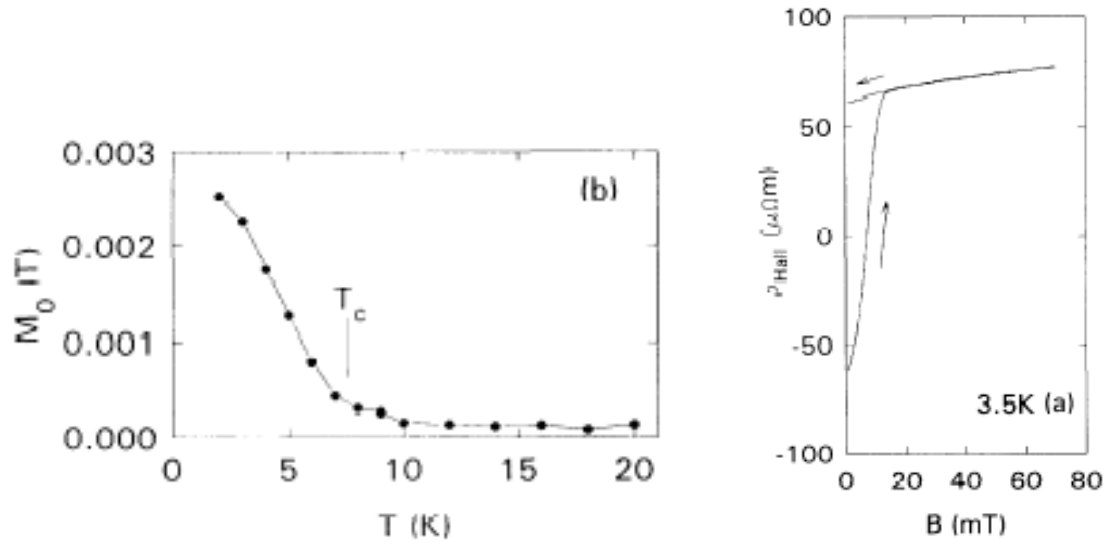


Fig. 13 Temperature dependence of the remnant magnetization (left) and a hysteresis of Hall resistance (right) observed in a *p*-type InMnAs film in 1991 [3].

From Hall measurements, one can conclude that a relatively low hole concentration (10^{19}) is necessary for mediating ferromagnetic exchange interaction in this system compared with its counterpart GaMnAs (10^{20}) [11].

Section 3-2 InMnAs-based heterostructures

III-V semiconductor heterostructures have served as a test bench for numerous new device concepts and revealed an array of new physical phenomena such as the integer and fractional quantum Hall effect. Ferromagnetic (In,Mn)As/(Al,Ga)Sb III-V heterostructures introduce a new dimensionality into normal semiconductor

heterostructures: magnetic long-range order. A critical temperature of 35 K was achieved in (In,Mn)As heterostructures in 1993 [4], much higher than (In,Mn)As thin films [3]. In addition, the lattice mismatch (0.6%-1.3%) between (In,Mn)As and (Al,Ga)Sb results in strain-induced, perpendicular magnetic anisotropy inside this system. The polar Kerr measurements of (In,Mn)As/AlSb heterostructures provided a direct proof for the perpendicular magnetization in this system [26], which is absent in (Ga,Mn)As/GaAs heterostructures. Typical polar Kerr rotation spectra for (In,Mn)As on various different buffer layers are shown in Figs. 14 and 15 [26]. Here, (In,Al)As buffer layers with different thickness was introduced to compensate for the lattice mismatch. Both polar Kerr measurements of saturation magnetization (upper panel in Fig. 15) and remnant magnetization (lower panel in Fig. 15) clearly show that the polar Kerr angle peaks are reduced when the thickness of (In,Al)As buffer layer is increased.

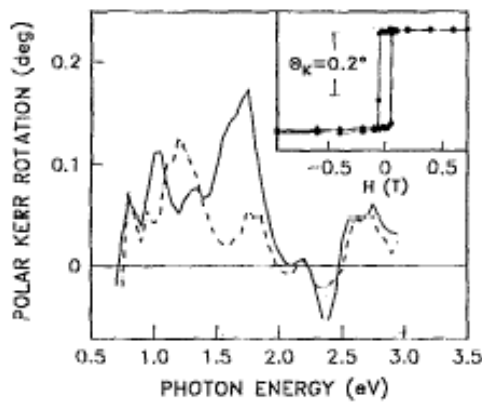
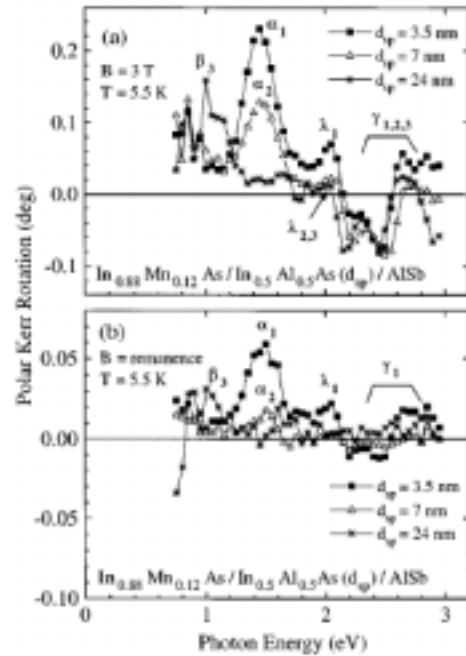


Fig. 14 Polar Kerr rotation spectra of at 5.5 K for two heterostructures: 9nm(19nm)-InMnAs/136nm(195nm)-AlSb. Inset shows a hysteresis loop at 1.75 eV. [26]

Fig.15 Polar Kerr rotation spectra at 5.5 K for different heterostructures showing saturation (upper panel) and remnant magnetization (lower panel) case. [26]



I mentioned in a previous chapter that two experiments have demonstrated the feasibility of controlling ferromagnetism in (In,Mn)As/(Al,Ga)Sb heterostructures [12,13]. There, heterostructures were essential to explain these long time accumulation effects in the experiments. Because of the type-II alignment of (In,Mn)As/(Al,Ga)Sb (see Fig. 16), a large built-in electric field exists, which can retain the holes inside the magnetic layers for a long time. That leads to a photoconductivity effect. That feature may be also the reason why such weak light intensity (5×10^{14} photons/cm²sec) used in Koshihara *et al.*'s experiment led to such a dramatic effect on ferromagnetic order [12].

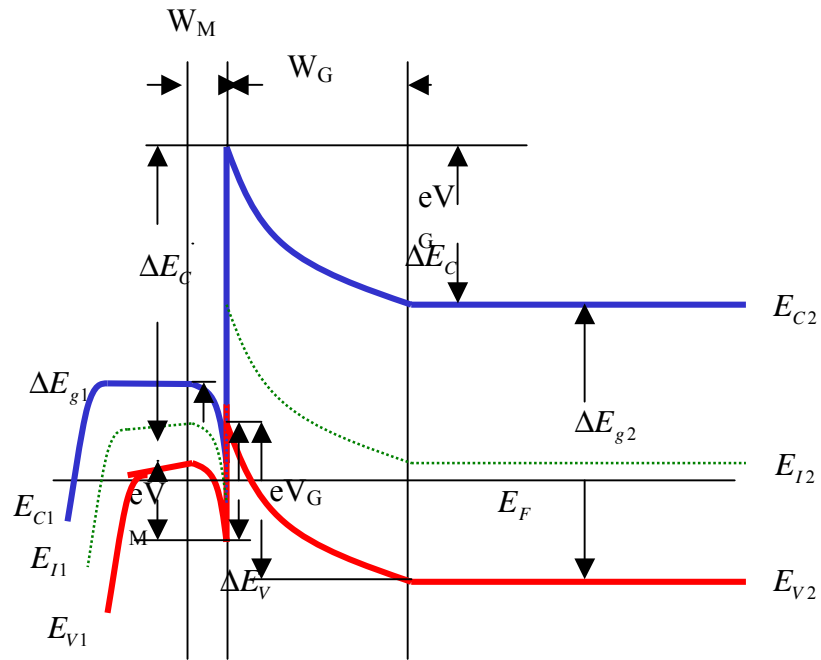


Fig. 16 Schematic band diagram of a type-II (In,Mn)As/(Al,Ga)Sb heterostructure. Due to a combination of the surface pinning of the Fermi energy and Mn doping, significant band bending exists.

The four MBE-grown heterostructures I have studied in this project are:

R1351: $\text{In}_{0.905}\text{Mn}_{0.095}\text{As}(9\text{nm})/\text{GaSb}(600\text{nm})$ on GaAs

K285: $\text{In}_{0.966}\text{Mn}_{0.034}\text{As}(15\text{nm})/\text{GaSb}(500\text{nm})$ on GaAs

K342: $(\text{In}_{0.53}\text{Ga}_{0.47})_{0.87}\text{Mn}_{0.13}\text{As}(50\text{nm})/\text{In}_{0.53}\text{Ga}_{0.47}\text{As}(100\text{nm})$ on InP

K22d: $\text{In}_{0.910}\text{Mn}_{0.090}\text{As}(25\text{nm})/\text{GaSb}(820\text{nm})$ on GaAs(100)

The Curie temperatures as well as the densities and mobilities of these samples are listed in Table I [30]:

Sample	Hole Density (cm^{-3})	Hole Mobility (cm^2/Vs)	Curie Temperature (K)
R1351	4.8×10^{19}	371	30
K285c	2.0×10^{19}	166	25
K342	$4-10 \times 10^{19}$	-	~ 110
K22d	1.1×10^{19}	323	55

Table I Characteristics of the four heterostructure samples I studied.

Charter 5 Experimental methods

In the current CW-MOKE/MCD and two-color time resolved MOKE experiments, the small or time-dependent transient change of the polarization is the signal of interest. Thus, any background noise (for instance, environmental coupling, electrical circuit noise...) should be carefully minimized. In this chapter I will describe the experimental methods and discuss the design idea for these experiments. The lasers used, the optical setups, the magnet system, the detection schemes and data acquisition schemes will be explained in detail.

In the CW MOKE/MCD experiment, the laser light was incident to the sample at an angle of less than 2.5 degrees from the sample normal. We used a He-Ne laser (632 nm), a Nd:YVO₄ laser (532 nm), and a 780 nm laser diode. An Oxford Spectromag-4000-10 superconducting magnet with optical access provided magnetic fields of up to 10 T at sample temperatures down to 1.2 K. The sample was mounted at the end of the sample stick, which is inserted into the variable temperature insert (VTI) fitted with ZnS windows, which separate the VTI from the outer vacuum can (OVC). Using a sensitive photoelastic modulator (PEM) and a polarization balanced bridge detection technique minimized the influence of the background noise. Frequency domain data acquisition technique is used here, where a phase-sensitive lock-in amplifier record the MOKE/MCD signal from a photodiode. Faraday rotation and dichroism response of the cryostat windows within the stray field of the magnet needed to be subtracted from the total signal in order to determine the true response of the sample. The details and the procedures of CW-MOKE/MCD experiments are presented next.

In the two-color time-resolved pump-probe MOKE experimental, intense MIR pulses from an optical parametric amplifier (OPA) are used to ultrafast create a lot of transit carriers only within the magnetic layer (InMnAs). A small fraction of energy from a chirp pulse amplifier (CPA) probes the ultrafast response of ferromagnetic order induced by those transient carriers. A polarization balanced bridge detection technique cancels the influence of the background noise. Time domain data acquisition technique, a Gated Integrator and Boxcar Averager, is used to minimize the effect of pulse-to-pulse fluctuations of intense MIR probe laser.

Section 5-1 Lasers

As stated in Chapter 4, the Kerr rotation angle and ellipticity strongly depend on the wavelength used since their magnitudes are determined by the electron spin polarization of the states participating in the magneto-optical transitions. In fact, the polar Kerr rotation spectrum of InMnAs/AlSb heterostructures has been shown to be strongly wavelength-dependent [26]. The spectrum is related to spin-polarized transitions involving Mn $3d$ states. Thus, it is important to choose the right photon energy as the probe in order to maximize our signal. We have used several lasers in our experiments. These include a He-Ne laser, a 780 nm laser diode, a Nd:YVO₄ diode pumped solid-state laser in the CW-MOKE/MCD experiment, and a chirped pulse amplifier (CPA) pumping an optical parametric amplifier (OPA) in two-color time resolved MOKE experiment. I will briefly review the features of these laser systems.

1. Laser diodes are commercially available compact laser sources, which take advantage of the current semiconductor technology and band structure engineering to design various heterostructures with various band gaps. Fabrication techniques such as MBE and MOCVD realize nearly single atom control. The ability to control the band gap allows one to choose the necessary output photon energy. Here we choose a 780 nm laser diode with output power 24 mW (Melles Griot 56-ICS-006). This system not only offers exceptional collimation and wavefront quality, but also their low-noise, constant-current driver and thermoelectric cooler controller ensure exceptional power and wavelength stability. A previous study showed that the maximum polar MOKE angle of InMnAs/AlSb heterostructures occurs at 1.65 eV (771 nm) [26], so it is reasonable to use a laser diode around 780 nm.

2. The most readily available laser sources one can obtain in optics labs are probably He-Ne lasers. They provide very good single color outputs (red) and are convenient for aligning optical paths. The output photon frequency is 632 nm. However, previous data indicate that the polar MOKE angle at this wavelength is small [26]. Also, considering the output stability and the small signal we want to measure here, He-Ne lasers are not serious used in the real measurements. We mainly used it to collinear with the MIR light to help align the optics.

3. Nd:YVO₄ is a solid-state laser. Our system is a Spectra-Physics Millennia. The output laser power is more stable than the He-Ne laser. A diode laser pumps active Nd³⁺ ions, which are doped in an yttrium vanadate crystalline matrix. It provides a 532 nm beam with cw power up to 5 W. We operated it around 0.2 W but a filter was necessary in order to prevent sample heating and protect the sample (neutral density filter with *OD*

= 1). At this wavelength, the expected MOKE angle for InMnAs/ (Al,Ga)Sb is about one-third of the maximum value [26]. So it is reasonable to observe the signal using this laser.

4. Chirped pulse amplifier (CPA) and optical parametric amplifier (OPA).

Chirp pulse amplification technique is widely used today to amplify the femtosecond laser pulses. When femtosecond laser pulses are to be amplified, the short pulses will lead to the high peak intensity which is very possible above the damage threshold of gain materials. This technique first stretches a pulse by a large factor (typically 10^5) and then safely amplifies the pulse. In the end, a pulse compressor is used to compensate the group velocity dispersion introduced in the previous steps and recompresses the pulse to the initial pulse duration.

In our two-color pump-probe MOKE experiment, a chirped pulse amplifier (CPA) (CPA-2001-Plus, Clark-MXR, INC.), which is based on chirp pulse amplification technique, is used as a probe. Fig. 17 shows the basic configuration of Clark CPA-2001-Plus system. Diode pumping (980nm) SErF femtosecond fiber oscillator provides femtosecond pulses with repetition rate in the 25 to 40 MHz range. These femtosecond pulses go through a pulse stretch and seed into a Ti: sapphire regenerative amplifier cavity. The gain medium is a Ti:sapphire crystal pumped by a frequency-doubled Nd:YAG laser. A build-in fast photodiode inside fiber oscillator cavity provides input signal to a Pockels Cell Driver, which generate reference signal to synchronize the timing of seed pulses, pump laser and cavity damping. Finally a pulse compressor compresses the amplified pulses to the duration of around 150fs.

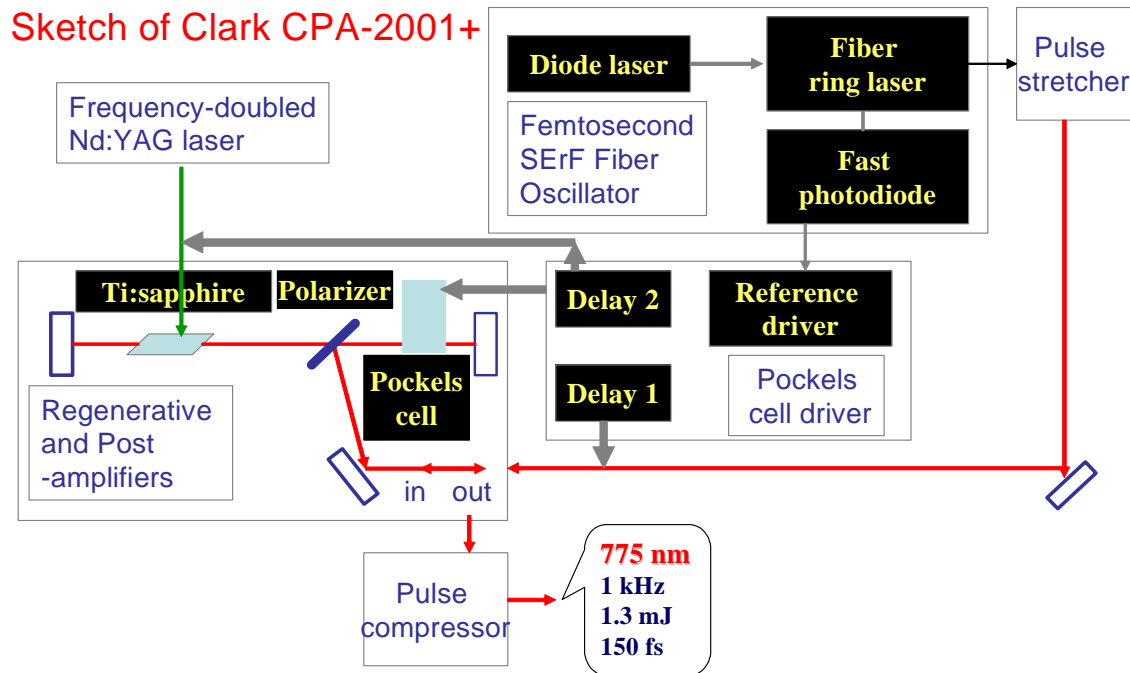


Fig. 17 Sketch of the Clark CPA 2001+ system.

A large fraction of energy from CPA pulses will pump an optical parametric amplifier (OPA), which serves as a pump to ultrafast create transit carriers within the magnetic layer. And a small fraction (around 10^{-5}) serves as a probe to detect the photo-induced ferromagnetic order change.

Optical parametric amplification (OPA) is a second-order nonlinear optical process and can produce tunable short pulses for a wide spectral range (for instance, from visible to MIR). The pump beam (775 nm, 150 fs, 1 kHz, 1.3 mJ) is the output of a chirped pulse amplifier (CPA) (CPA-2001-Plus, Clark-MXR, INC.), which is essentially a Ti: Sapphire regenerative amplifier system as described above. Our OPA system

(Quantronix/Light Conversion's TOPAS) can provide tunable light from 200nm to 20 μm (See the first Fig.18).

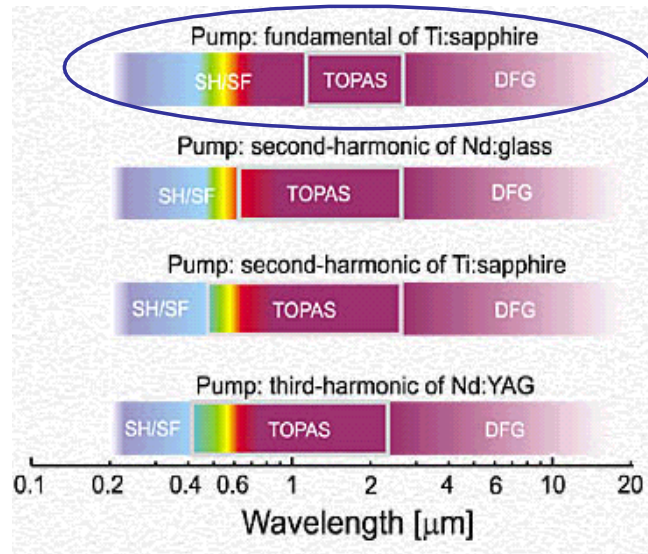


Fig. 18. Tuning range of different operation modes of Quantronix/Light Conversion's TOPAS. First row is applicable to the OPA system in our lab. (Download from web page of Light Conversion, Ltd.)

In the first step of the OPA, a small part of the pump beam (Pump 1) generates superfluorescence in the nonlinear crystal (BBO). A small part of the spectrum at the desired wavelength is selected by a grating and then amplified in the next four stages of the OPA. For our purposes, this computer controlled ultrafast OPA (Quantronix/Light Conversion's TOPAS) is used to provide 2 to 3.1 μm , 150 fs, 1.5 μJ laser pulses for creating large densities of transient carriers only within the magnetic layer of InMnAs/GaSb heterostructures. This particular wavelength range of the OPA is perfect

for studying transient carrier-induced ferromagnetism phenomena in these narrow gap InMnAs/GaSb DMS heterostructures.

Section 5-2 Superconducting magnet system

An Oxford Spectromag-4000-10 superconducting magnet is used in this project. The superconducting split-pair, horizontal-field magnet system provides optical access to a sample in a variable magnetic field and low temperature environment. Schematic pictures of the magnet system downloaded from their website (<http://www.oxinst.com>) are shown in Fig. 19.

This system can provide magnetic fields up to 10 Tesla. Our sample is mounted on the sample stick inside the variable temperature insert (VTI). The VTI can provide sample temperature control from 1.2 K to 300 K by balancing Helium flow with an inside heater. The rectangular tail of the magnet provides excellent optical access to the sample.

The VTI is isolated from outside by an outer vacuum can (OVC) with four optical windows. The windows allow measurements from the visible to the far infrared by choosing different window materials. For example, in our time-resolved experiment, in which 3 μm pump light is used, the VTI window of choice is ZnS. The OVC windows are CaF_2 . These optical elements induce finite Faraday rotation and dichroism due to the stray field of the magnet, which add to the real MOKE/MCD signal from the sample. We used an aluminum mirror to make a reference measurement of the background Faraday rotation and dichroism. A correct MOKE signal was then obtained by subtracting the reference signal from the sample measurement signal.

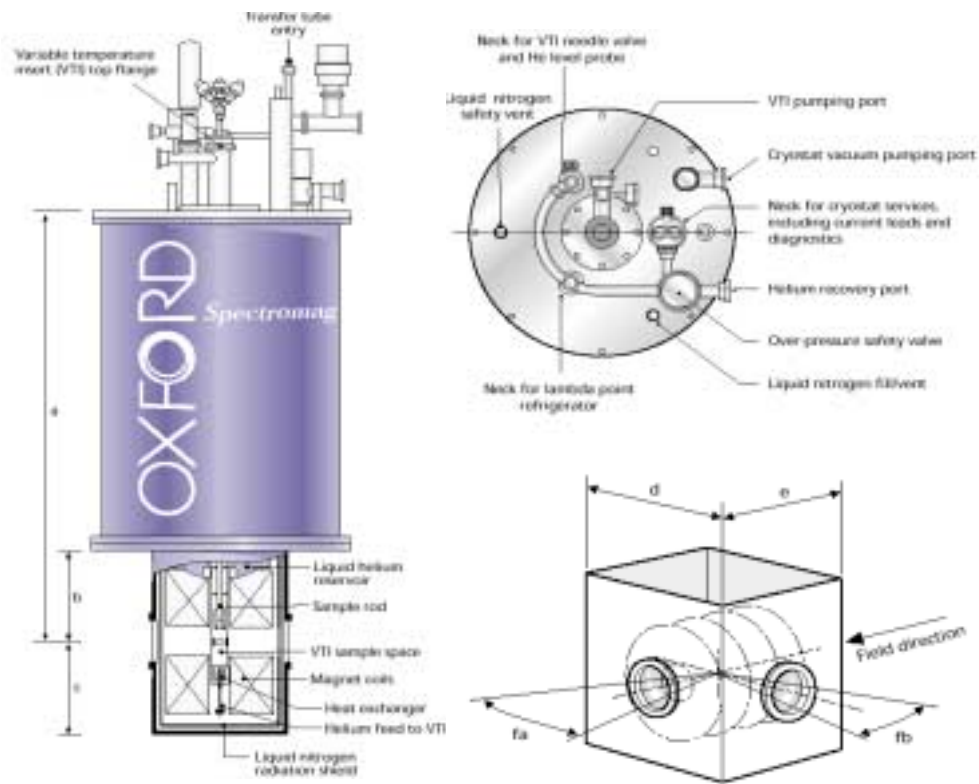


Fig. 19 Sketch of the Oxford Spectromag-4000-10 superconducting magnet. (Downloaded from www.oxnist.com.)

Section 5-3 Optical setups

Schematic diagrams for the optical setups for CW MCD, CW MOKE, and time-resolved MOKE are shown in Figs. 20, 21 and 22, respectively. I will explain the design idea and optical components used in these experiments separately in the next three subsections.

5-3.1 Optical setup for the CW-MCD experiment

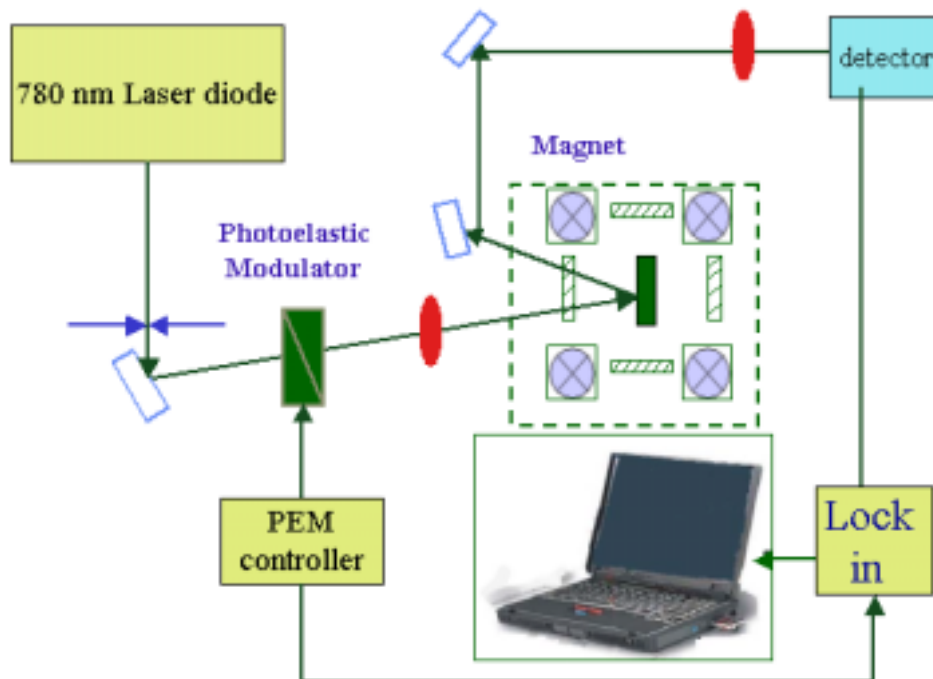


Fig. 20 Schematic diagram for the CW MCD experimental setup.

The setup for measuring MCD is depicted in Fig 20. It is quite simple and the diagram should be self-explanatory. Three light sources were used here (He-Ne laser, Spectra-Physics Millennia Nd:YVO₄ Laser and Melles Griot 56-ICS-006 laser diode). A photoelastic modulator (PEM) system (Jasco, Inc) was used for detecting MCD signal. The PEM modulated the light polarization at a frequency of ~ 50 kHz. The principle of Jasco PEM system will be discussed in the detection schemes section. A photodiode detector/preamplifier (DET-90-004-Si-PV, Hinds Instruments, Inc) served as a detector for the PEM system. The other optical elements included several gold-coated mirrors and lenses for steering and focusing the beam, respectively. The sample was mounted in the

sample chamber of the Oxford magneto-optical cryostat with a split-coil superconducting magnet, as stated above. It was hit by the light beam at near normal incidence (smaller than 3 degree). The dichroic response of the cryostat windows within the stray field of the magnet was taken into account by deducing the signal of the sample from the signal of a mirror. Finally, the detector signal was read by a lock-in amplifier (Stanford Research System, 830), which was locked at the PEM modulation frequency.

5-3.2 Optical setup for the CW-MOKE experiment

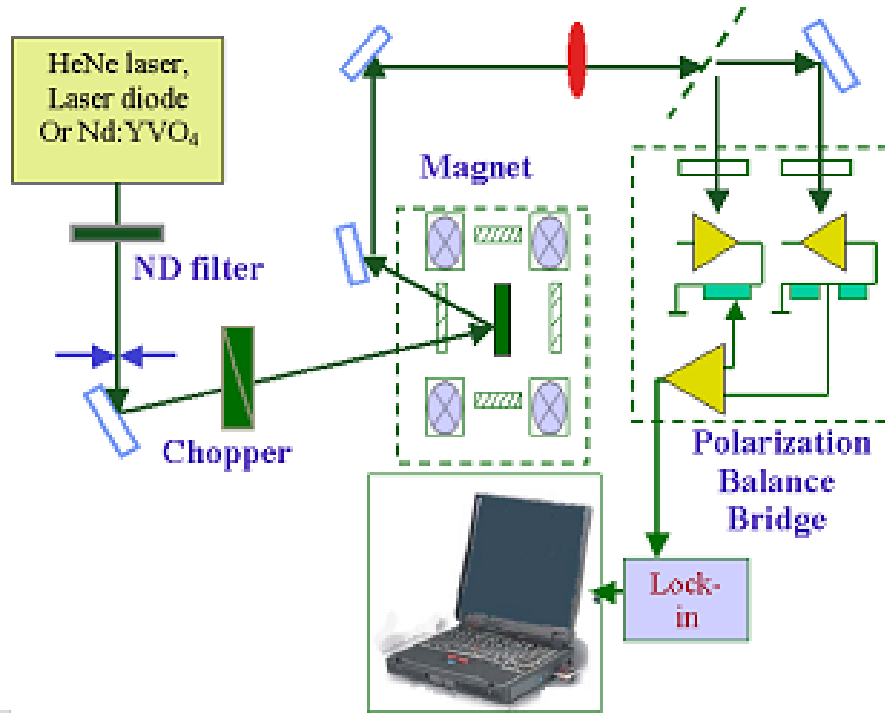


Fig. 21 Schematic diagram for the CW-MOKE experimental setup.

The optical setup for measuring MOKE in cw is depicted in Fig. 21. Here, as in the CW-MCD experiment, three laser source and detector arrangements were used. In order to observe a large polar MOKE angle, the angle between the input beam and the

sample normal was kept smaller than 2.5 degrees. An optical chopper (Thorlabs, Inc.) was used to modulate the light intensity at 500 Hz. A Wollaston prism served as a polarization-dependent beam splitter, which spitted the linearly polarized beam into two parts, each with 50% intensity of the original beam. Next a polarization balance bridge scheme was used to detect a polar Kerr signal, which will be explained in the detection schemes section. The idea is sketched in Fig. 19. The output signal from a pair of equivalent photodiodes (Nirvana-2007, New Focus, Inc.) was recorded at 500 Hz with a lock-in amplifier.

5-3.3 Optical setup for the time-resolved MOKE experiment

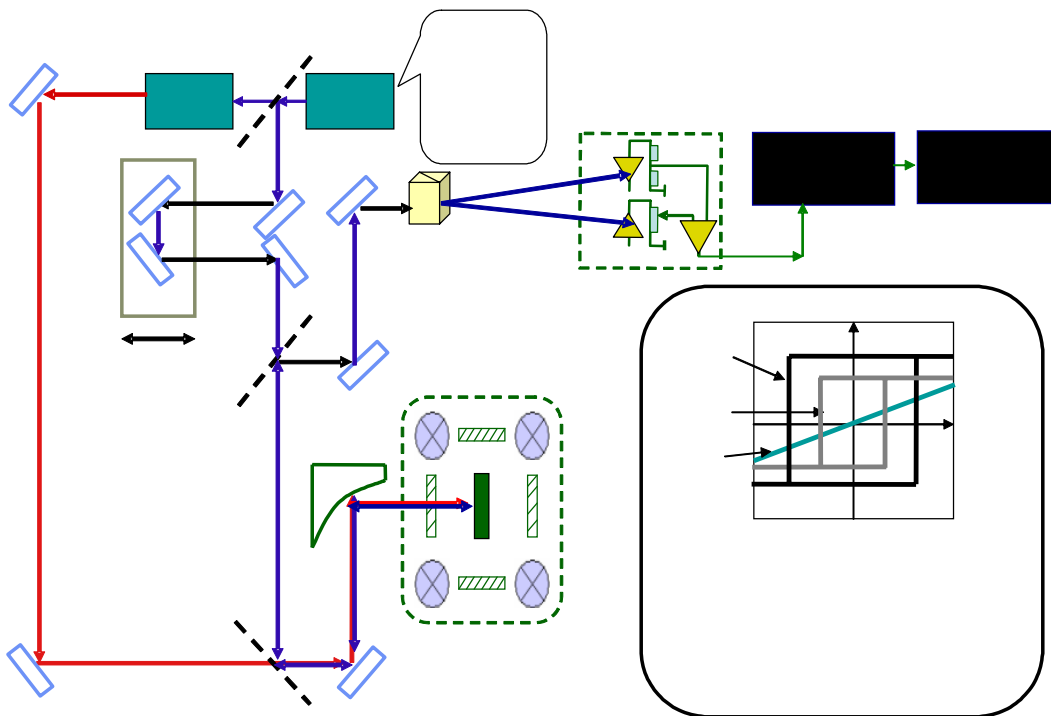


Fig. 22 Schematic diagram for the time-resolved MOKE spectroscopy setup.

In this subsection, I will discuss our two color time-resolved pump-probe MOKE experimental setup. The NIR beam (775 nm) from the CPA (CPA-2001-Plus, Clark-MXR, INC.) will be used as a probe and the MIR beam from the OPA (Quantronix/Light Conversion's TOPAS) will be used as the pump. The pump wavelength (2 to 3.1 μm) is chosen in such a way that we only create transit carriers within the magnetic layers, which allow us to study the ultrafast carrier-induced ferromagnetic order change inside the sample in sharp contrast to the persistent photoconductivity effect in the previous study.

The setup for the time-resolved MOKE experiment is depicted in Fig. 22. The idler mode or different frequency generation (DFG) mode of the OPA serves as a pump with pulse duration 150 fs and wavelength 2 to 3.1 μm . In the current experiment, 2 μm pump light wavelength is chosen. Since the photon energy is close to the InMnAs band gap and smaller than any other band gaps in the structure be used to create a large density of transient carriers only within the magnetic layer of the sample. A parabolic mirror focuses the pump light into the sample. The pump-probe MOKE experiment will be carried out in a polar Kerr configuration. The probe pulse from the CPA has a wavelength of 775 nm, which is close to the maximum polar Kerr angle of the sample. A Wollaston prism is used as a beam splitter to split the reflected probe pulse into two spatially separate components and detected by a balanced detector (Nirvana-2007, New Focus, Inc.). A Gated Integrator and Boxcar Averager (SR250, Stanford Research Sys, INC) is used to record signal. Through this way, I could detect small pump-induced polarization changes inside the DMS layer and mapped time evolution of photo-induced nonequilibrium ferromagnetism.

Finally, I would like to present an estimate on how many carriers will be created inside the magnetic layer with our design. The parameters and abbreviations used in the calculation are listed below:

W : pulse energy of the pump; τ : pulse width of the pump; λ : wavelength of the pump; r_0 : radius of the Gaussian beam before focusing by a parabolic mirror; r : radius of the Gaussian beam after focusing by a parabolic mirror; I_0 : incident light intensity to the sample; I : light intensity after transmitting through the sample; l_0 : sample thickness; and α : absorption coefficient; K : imaginary part of the index where $\alpha = 4\pi K / \lambda$; f : focal length of the parabolic mirror.

The values I used for these parameters in my estimate are: $W = 2 \times 10^{-6}$ J; $\tau = 150$ fs; the repetition rate: 1 kHz; $r_0 = 0.35$ inches; the energy gap of (InMn)As $E_g = 0.41$ eV; $K = 0.102$, $\alpha = 4.3 \times 10^3$ /cm, $l_0 = 1 \mu\text{m}$, $f = 6$ inches.

According to geometric Gaussian optics, the radius of a Gaussian beam after focusing by a parabolic mirror with focal length f is given by

$$r \equiv \left(\frac{2\lambda}{\pi} \right) \left(\frac{f}{2r_0} \right).$$

The illuminated area and the intensity of the incident beam on the sample are $S = \pi r^2$ and $I_0 = W / (\tau * S)$, respectively. From these, the density of the carriers created by the pump can be expressed as

$$n = W(1 - e^{-\alpha l_0}) / (\hbar \omega * S * l_0).$$

Inserting the relevant parameters in this formula, we get Table.II.

R (cm)	I_0 (J/s*cm ²)	S (cm ²)	n (cm ⁻³)
$1.64*10^{-3}$	$1.58*10^{12}$	$0.85*10^{-5}$	$1.28*10^{22}$

Table II. The relevant parameter estimations in pump-probe MOKE experiment

Typical Mn concentrations N_{Mn} of (In,Mn)As DMS heterostructures are on the order of 10^{21} cm⁻³ (for instance, $N_{Mn} = 10^{21}$ for In_{0.94}Mn_{0.06}As [12]). Thus from our estimate above and Fig. 9 in the theoretical review section, we can conclude that the current proposed time-resolved pump-probe MOKE experiment can probe the physics across the boundaries of the different regimes in the time domain, which should shine new light on the existing theoretical controversies and bring new, exciting experimental results.

Section 5-4 Detection schemes

In order to achieve high precision polarization measurements, two schemes are employed: a polarization balanced bridge technique and a photoelastic modulator (PEM) technique.

- Balance polarization bridge technique: the basic idea is as follows (see Fig. 19). A linearly polarized laser beam is reflected from the sample and goes through a non-polarizing beam splitter, which splits the beam into two parts, each with 50% and 50% intensity of the original beam. The two beams then pass through analyzers. The polarization planes of the two analyzers are 45 degrees with respect to the input laser polarization and 90 degrees to each other. Next, two photodiodes, which are used in a photoconductivity configuration, provide input

to preamplifiers. After that, the output of the preamplifiers provides input to a differential amplifier. A lock-in amplifier measures the signal from the output of the differential amplifier with different gains. A chargeable battery provides power for the circuits and detectors. We have tried different combinations of beam splitter and detector in our CW-MOKE experiments, but we finally chose the combination of a Wollaston prism and a New Focus balance detector (Nirvana-2007). The Wollaston prism serves as a beam splitter to split the reflected beam into two spatially separated components with polarization directions orthogonal to each other. The New Focus balance detector serves as a pair of equivalent detectors and differential preamplifier. The feedback loop in the Nirvana detector splits the reference photodetector current, I_R , to generate the cancellation photocurrent (see Fig. 23).

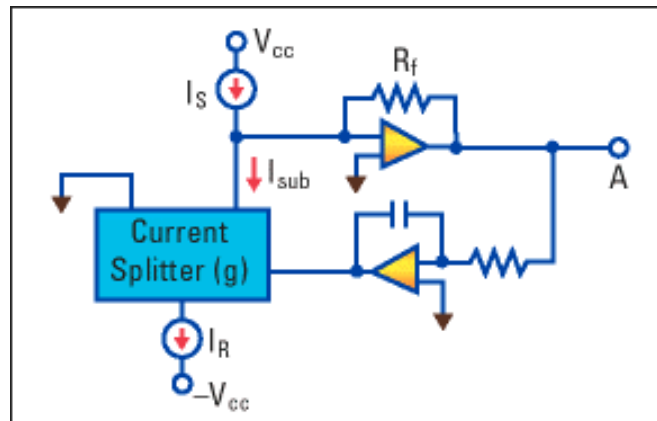


Fig. 23 Schematic diagram of the circuit used in the New Focus Nirvana detector feedback loop. The idea here is to split the reference photodetector current, I_R , to generate the cancellation photocurrent. Figure downloaded from the New Focus website (www.newfocus.com).

- Photoelastic modulator (PEM) technique: We measured MCD by using a photoelastic modulator (PEM). A PEM directly modulates the relative phase velocity of one optical axis to another, allowing high precision light polarization measurements of various types. The basic working principle is as follows: if a sample of transparent solid material is stressed by compression or stretching, the material becomes birefringent. That is to say, different linear polarizations of light have slightly different speeds of light when passing through the material. A piezoelectric transducer is attached to the transparent sample and controlled by a driving circuit to provide phase modulation of light.

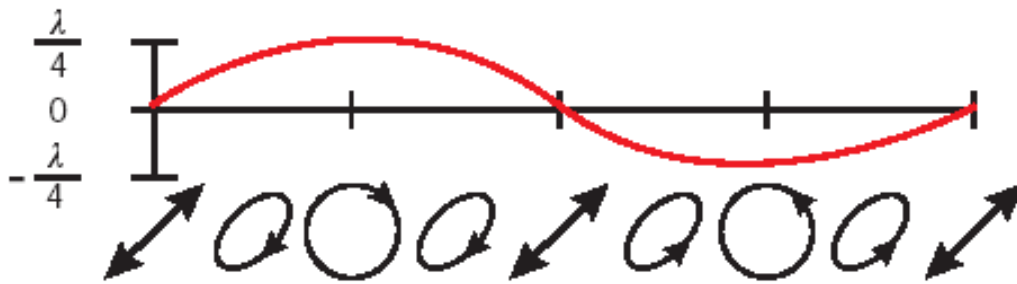


Fig. 24 One cycle of quarter wave modulation using a photoelastic modulator. Figure downloaded from HINDS INC. website (www.hindspem.com).

In our case, quarter wave retardation is used to measure the MCD signal (see Fig. 24). In one cycle of quarter wave modulation, the PEM modulates the incident linear polarized beam (45 degrees with respect to the optical axis of the PEM) from left circularly polarized light to right circularly polarized light. Thus, for such a setup, ac coupling of the $1f$ signal from the lock-in is the MCD signal from the sample.

Section 5-5 Data acquisition schemes

- Frequency domain detection technique

In the CW-MCD/MOKE experiment, we adapted a lock-in amplifier (SR 830, Stanford Research System, Inc) to record the signal. This is based on a well-known phase sensitive detection technique. Basically speaking, a lock-in amplifier will only be sensitive to the component of the signal which has the same *frequency AND phase* as the reference. External modulation from a mechanical chopper or a Photoelastic Modulator (PEM) was used to provide the reference frequency to the lock-in amplifier. Through this simple method, we successfully record the MOKE/MCD signal.

- Time domain detection technique

In order to perform two-color time resolved measurements, I need to use our fs laser pulses as probe to detect small MOKE signal. On the one hand, our fs laser CPA is an intense MIR light source with pulse-to-pulse fluctuations of a few percent. Such a noise background will suppress the small MOKE signal which is interested in here. On the other hand, the repetition rate of our CPA system is 1 KHz, which is not compatible with high frequency modulation scheme. So we decided to use time domain data acquisition technique.

Gated Integrator and Boxcar Averager system (SR250, Stanford Research System, Inc.) is a modular instrumentation system which is extreme useful to recover small, fast analog signal from large noise background. The signal

interested here is only existed in the pulse duration of 150 fs with the repetition rate of 1 KHz. By choosing the proper gate width and delay time of data acquisition, one can only take data within the time when the real signal does exist (see Fig.25). By exponential averaging 1000 pulses using a Boxcar Averager, we will improve the signal to noise ratio around the factor of 30 since the summation of the noise will follow a random walk manner instead of monochromic increase in the real signal case. Through this way, the small MOKE signal is extracted out of the large noise background.

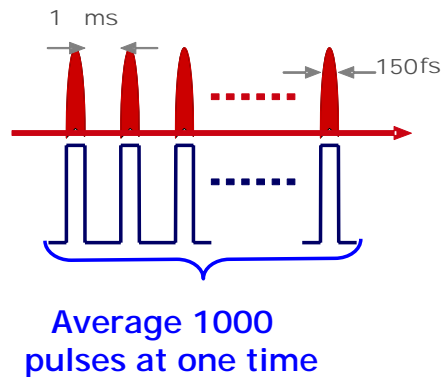


Fig. 25 Simple sketch of idea of a Gated Integrator and Boxcar Averager.

Using the polarization balanced bridge technique and PEM technique described above, with the help of phase sensitive data acquisition technique or time domain detection technique, we have detected the MOKE/MCD signals proportional to the Kerr rotation (MOKE) and ellipticity (MCD), respectively. Both are proportional to the magnetization perpendicular to the sample surface, and hence, the magnetic properties of (In,Mn)As DMS heterostructures can be probed this way.

Charter 6 Results and discussion

Section 6-1 CW MCD measurements

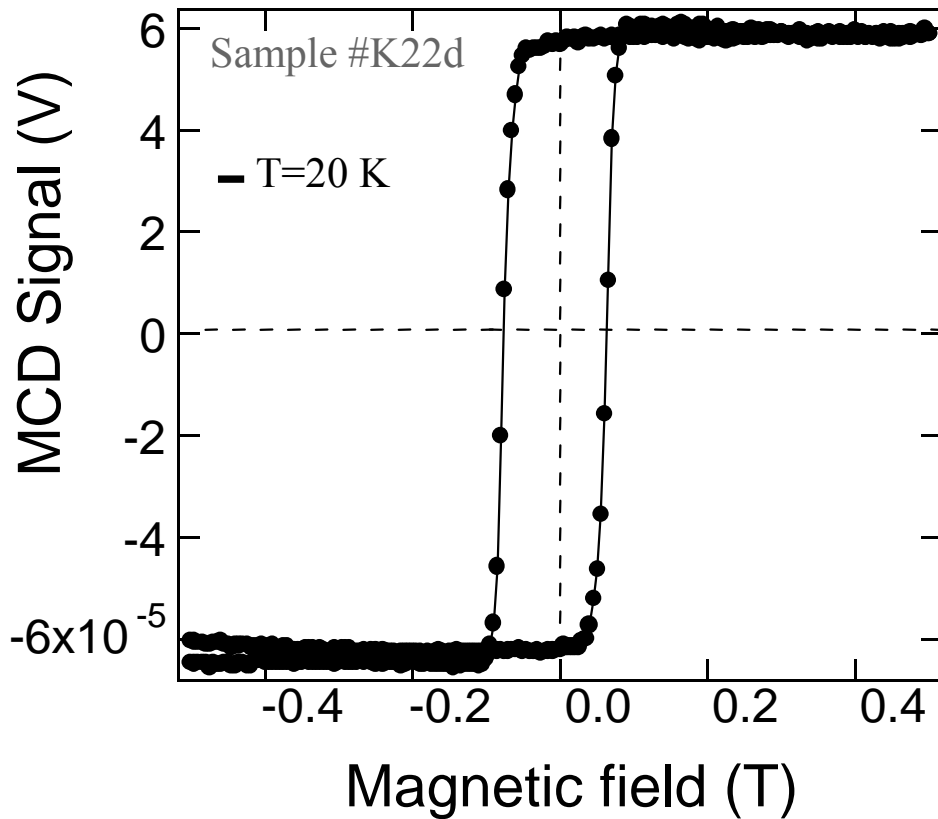


Fig. 26 Typical MCD hysteresis trace obtained for K22d ($T = 20$ K, probe laser wavelength = 780 nm).

Figure 26 shows a typical magnetization curve obtained for sample K22d at 20 K using the MCD setup (see Fig. 20) with the PEM detection scheme and phase sensitive data acquisition technique. The structure of the sample K22d is $\text{In}_{0.910}\text{Mn}_{0.090}\text{As}(25\text{nm})/\text{GaSb}(820\text{nm})$ on $\text{GaAs}(100)$. The data was taken with the 780 nm laser diode and the magnetic field was applied perpendicular to the surface, i.e., along

the easy axis. The observed polar Kerr hysteresis loop is a nice demonstration of ferromagnetic order of (In,Mn)As heterostructures. This data also suggests that the InMnAs/GaSb heterostructure has strong perpendicular magnetic anisotropy, which leads to a near squareness of the hysteresis loop; i.e., the MCD signal at zero magnetic field is almost equal to the signal at 0.5 T (Fig.26). This high squareness indicates that paramagnetic contributions are almost negligible to the MCD signal. A coercive field H_c of 0.065 T is deduced from the data in Fig. 26 for K22d at 20K. This coercive field can be understood in terms of domain wall energy, which includes three parts: exchange energy, anisotropy energy and a Zeeman energy term. This value indicates how easy one can flip the spin inside a ferromagnet below its Curie temperature. One can also define a ferromagnetic material is a “soft” ferromagnet or “hard” ferromagnet using this parameter.

The MCD measurements of the other two samples K285 and R1351 are also successful performed (figure 27 and figure28) with the same PEM detection scheme. The structures of two samples are $\text{In}_{0.905}\text{Mn}_{0.095}\text{As}(9\text{nm})/\text{GaSb}(600\text{nm})$ on GaAs for R1351 and $\text{In}_{0.966}\text{Mn}_{0.034}\text{As}(15\text{nm})/\text{GaSb}(500\text{nm})$ on GaAs for K285, respectively. The lattice mismatch leads to strong perpendicular magnetic anisotropy in these two samples, which is a common feature in this heterostructure system. Thus, our discussion of K22d is also applicable here.

The MCD data shown in Fig.27 for K285 was taken at temperature 10.6K. A coercive field of 0.07 T can be deduced. The MCD data shown in Fig. 28 for R1351 was taken at temperature 20K. A coercive field of 0.08 T can be seen from the figure.

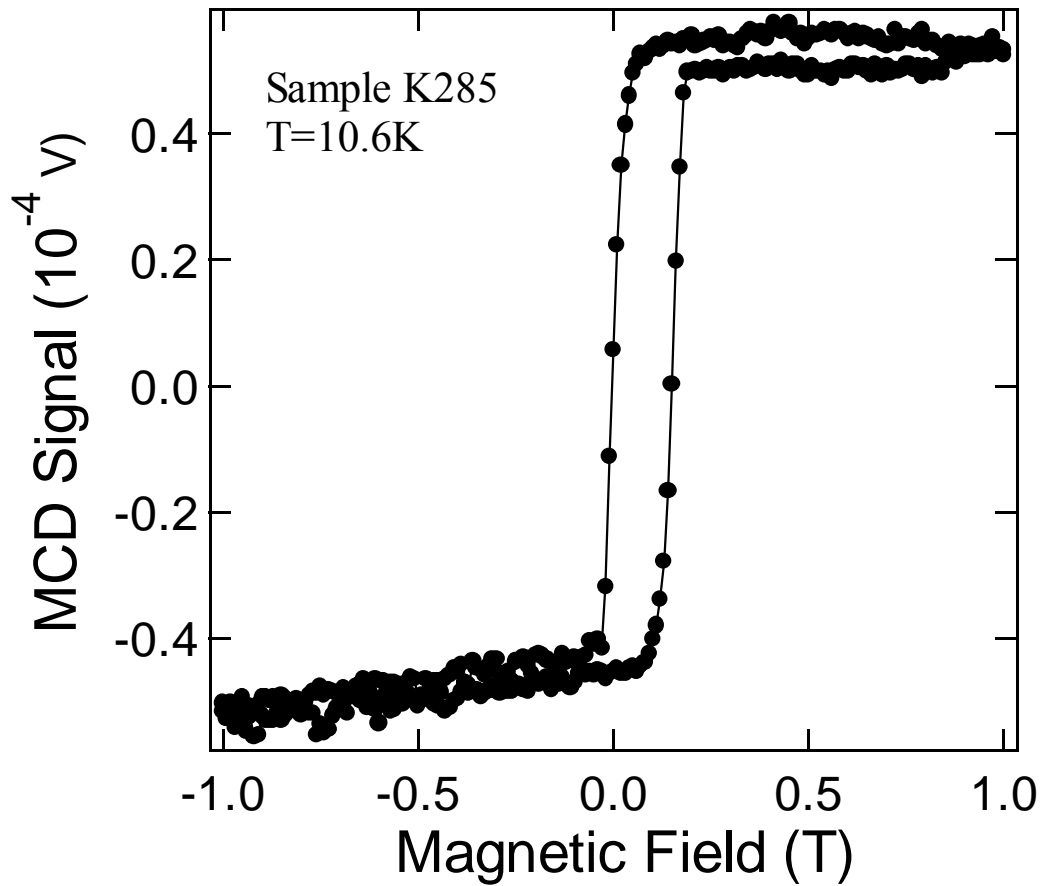


Fig. 27 Typical MCD hysteresis trace obtained for K285 ($T = 10.6$ K, probe laser wavelength = 780 nm).

In the Figs. 26, 27 and 28, the vertical offset, which is due to the dichroism of other optical elements inside the optical path, have been subtracted easily. More problematic is the presence of a horizontal offset in Figs. 27 and 28, which is not seen in Fig. 29. The origin of this feature is not consistent with SQUID measurement and is still an open question at this point.

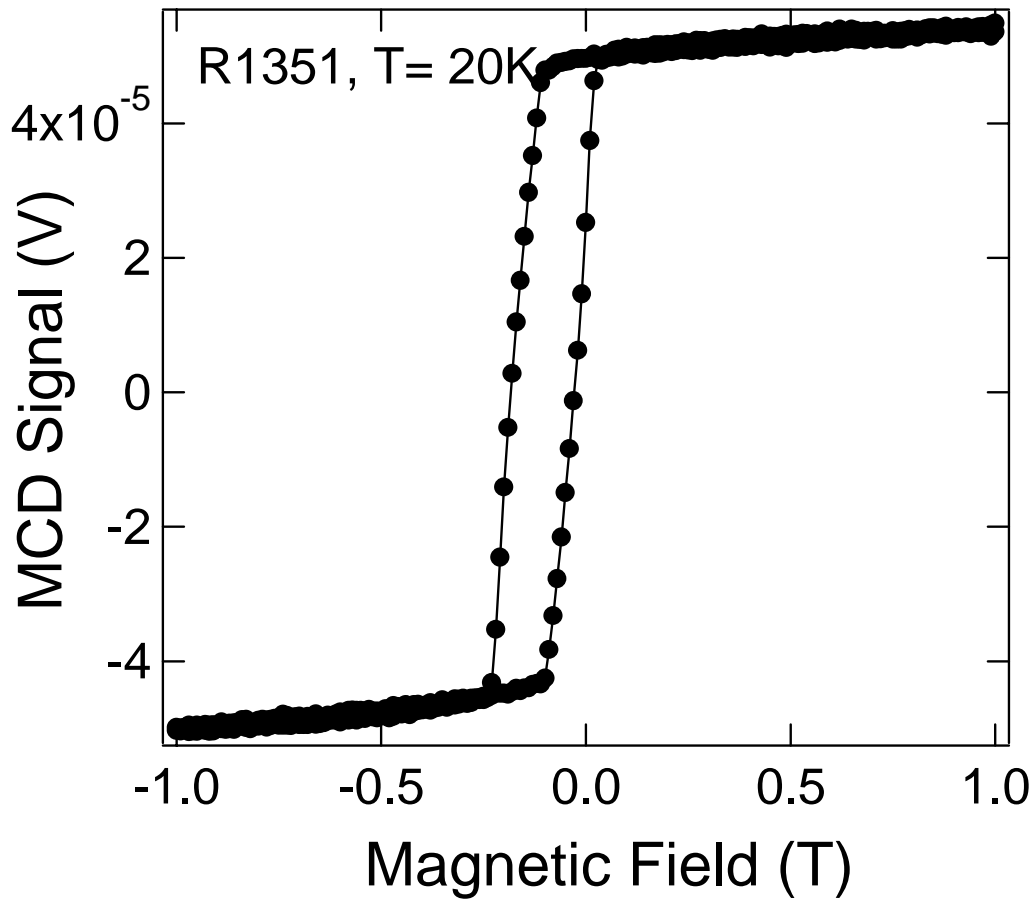


Fig. 28 MCD curve for Sample R1351 using the 780 nm laser diode at 20 K.

We were also able to observe hysteresis loops by using a Nd:YVO4 laser described earlier with a wavelength of 532 nm. The hysteresis loop shown in Fig. 25 was taken for R1351 at $T = 2.2$ K with this laser. Although the loop is obviously noisier than the loop using the laser diode due to the smaller signal size expected for this wavelength in InMnAs/(Al,Ga)Sb heterostructures, the hysteresis is still clear.

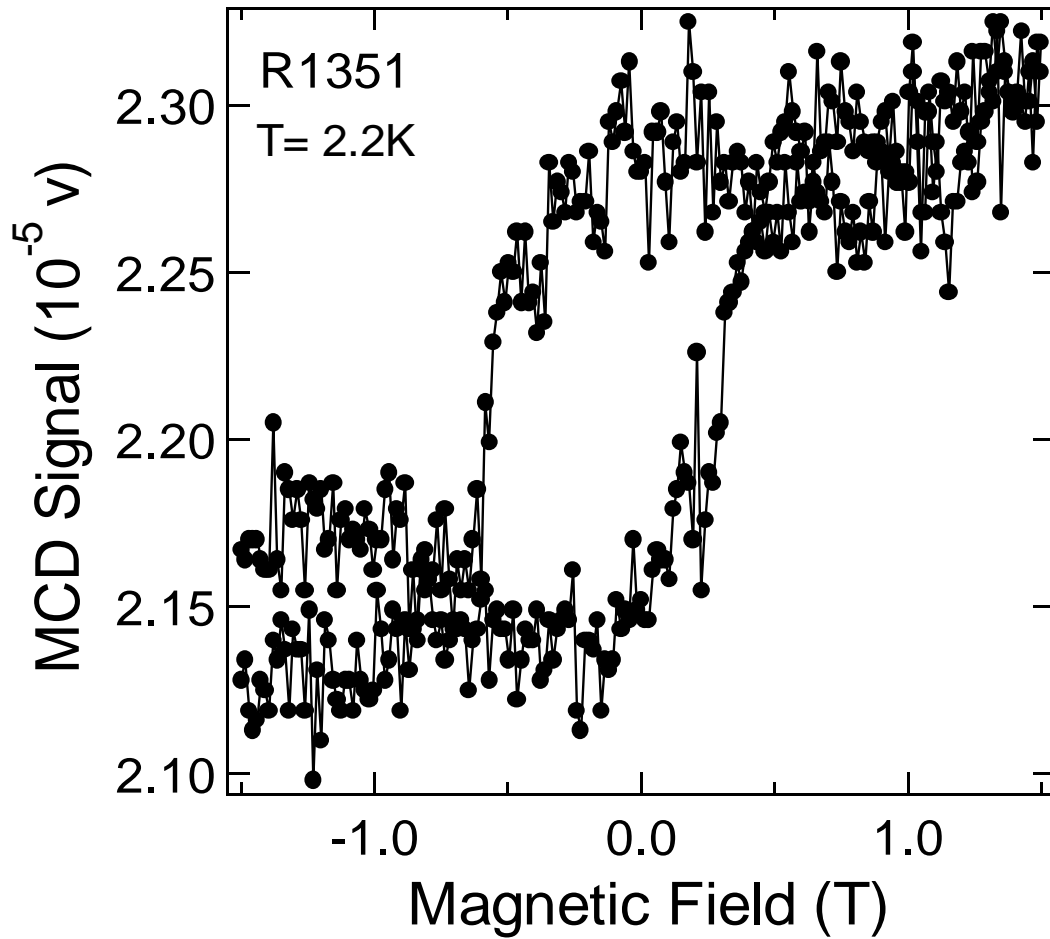


Fig. 29 MCD curve for sample R1351 using the 532 nm laser at 2.2 K

I also performed the MCD measurements on sample K342 using the same polar Kerr configuration setup (the applied magnetic perpendicular to the sample surface). However I was unable to see any ferromagnetic hysteresis loop hysteresis below its Curie temperature. This is due to the fact that the magnetic easy axis of K342 is in the plane of the sample surface instead of perpendicular to the sample surface. The sample structure of K342 is $(\text{In}_{0.53}\text{Ga}_{0.47})_{0.87}\text{Mn}_{0.13}\text{As}(50\text{nm})/\text{In}_{0.53}\text{Ga}_{0.47}\text{As}(100\text{nm})$ on InP. This is a new type of III-V DMS heterostructure grown only recently and T_c as high as 120K. The very small lattice mismatch among (In,Ga)MnAs, (In,Ga)As and InP results in almost

strain-free interfaces inside the structure, which leads to in-plane magnetic anisotropy.

Current Polar Kerr measurement setup is not suitable to study this sample.

Section 6-2 Temperature dependence of MCD

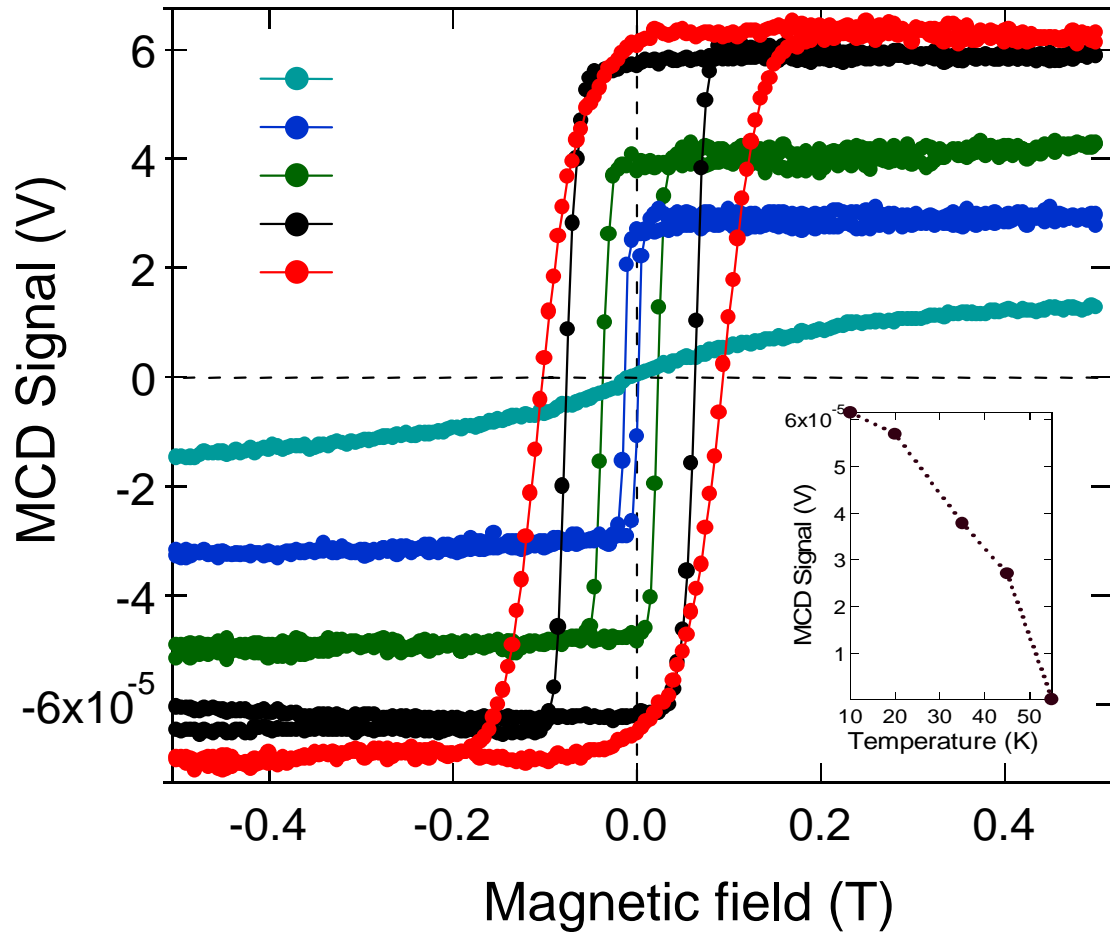


Fig. 30 MCD signal vs. magnetic field at seven different temperatures obtained for K22d using the 780 nm laser diode. It can be seen that the size of the hysteresis loop, and therefore the MCD signal at zero external field, decreases with increasing temperature. Inset shows MCD signal at zero field vs. temperature. T_c is around 55K can be deduced from this curve.

Figure 30 shows the temperature dependence of the MCD signal obtained for sample K22d. The data was taken with the 780 nm laser diode also. MCD signal vs.

magnetic field for the heterostructure sample at five different temperatures are plotted in the same graph. In addition, inset of Fig. 30, the MCD signal at zero field (i.e., in the presence of the remnant field) is plotted against temperature.

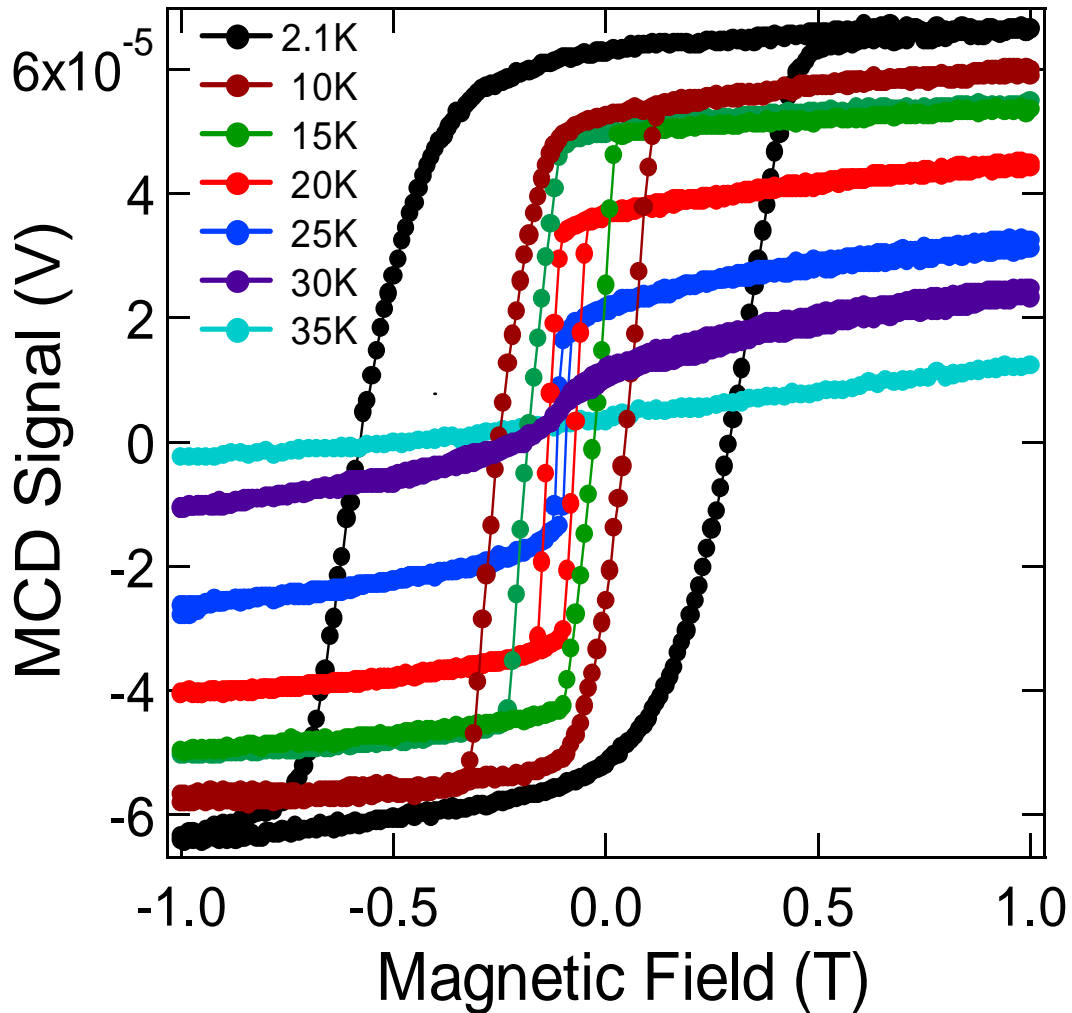


Fig. 31 MCD signal vs. magnetic field at seven different temperatures obtained for R1351 using the 780 nm laser diode. It can be seen that the size of the hysteresis loop, and therefore the MCD signal at zero external field, decreases with increasing temperature.

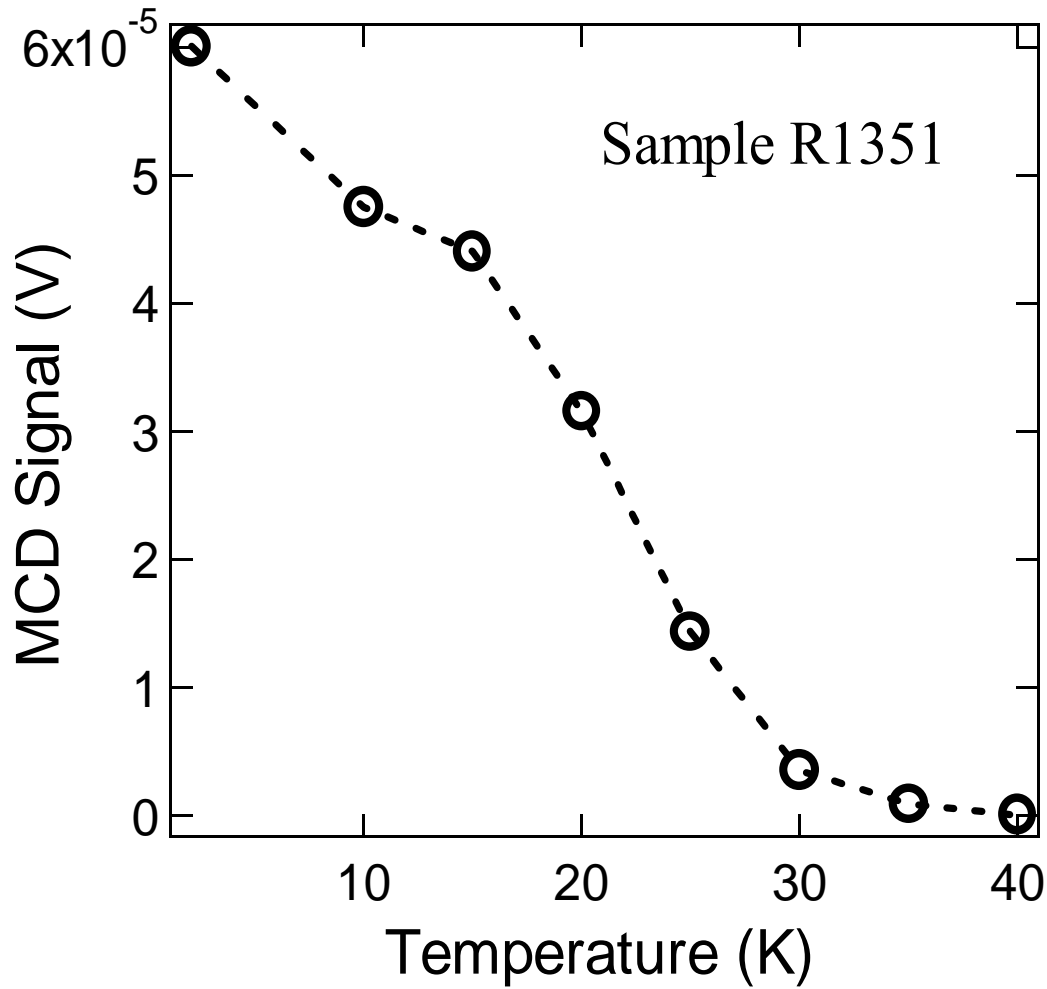


Fig. 32 The temperature dependence of the zero-field MCD signal for R1351 using the 780 nm laser diode. $T_c \sim 30$ K can be deduced from this curve, consistent with Hall and SQUID data [30].

The ferromagnetic transition temperature T_c deduced from inset of Fig.30 is 55 K, which is the consistent with the data obtained in Hall measurements and magnetization measurements using a SQUID [30]. This is the highest Curie temperature sample existing in InMnAs to date.

Next two figures (Fig. 31 and Fig. 32) show the temperature dependence of the MCD signal obtained for sample R1351. The data was taken with the 780 nm laser diode also. Figure 31 shows MCD signal vs. magnetic field for the heterostructure sample at

seven different temperatures. In addition, in Fig. 32, the MCD signal at zero field (i.e., in the presence of the remnant field) is plotted against temperature. The ferromagnetic transition temperature T_c deduced from these figures is 30 K.

Similarly, MCD data were taken for sample K285 using the 780 nm laser diode at four different temperatures. The obtained four hysteresis loops are plotted in Fig. 33. From this we can conclude that the critical temperature of K285 is around 25K. All this data obtained here are consistent with previous Hall measurements and SQUID measurements.

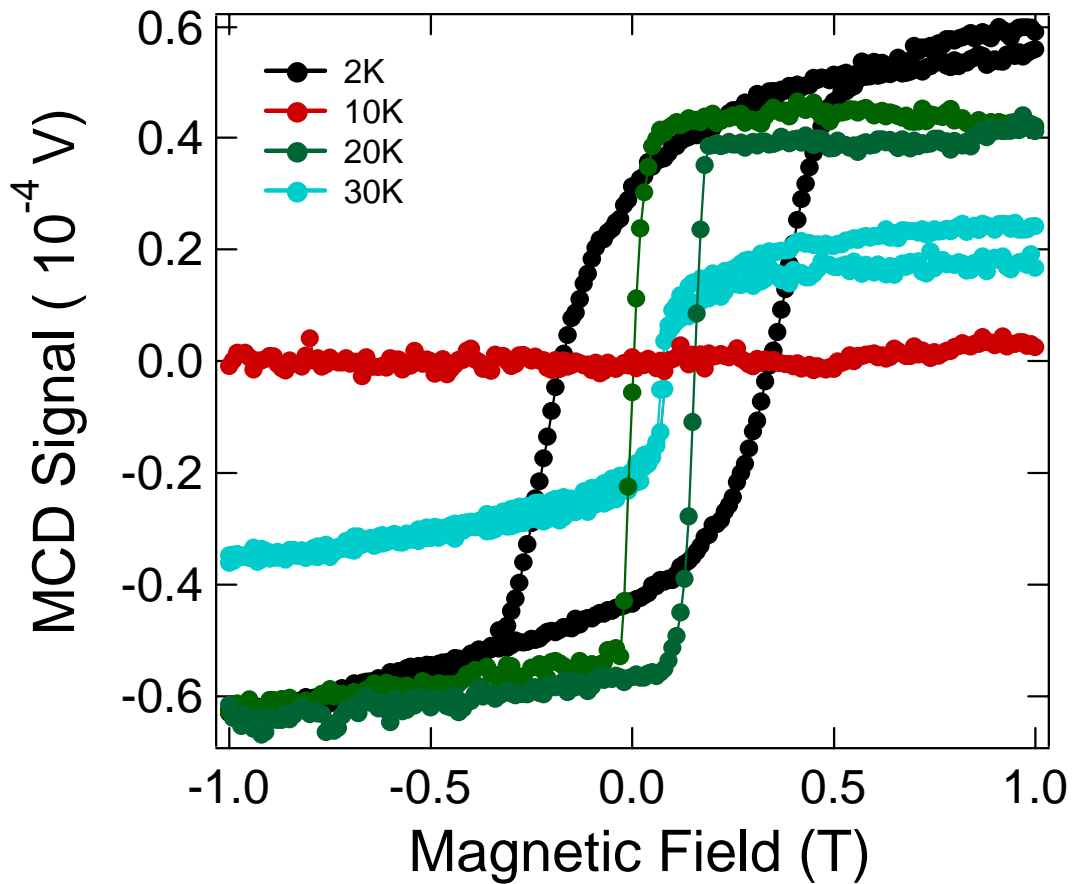


Fig. 33 MCD signal vs. magnetic field at four different temperatures obtained for Sample K285 using the 780 nm laser diode.

Section 6-3 CW-MOKE data

Shown in Fig. 30 is one example of CW MOKE data of sample K22d at 20 K using the 780 nm laser diode in conjunction with the New Focus balanced polarization bridge detector (Fig. 21). We can clearly see a hysteresis loop. An aluminum mirror reference signal of the background Faraday rotation was subtracted from the output signal

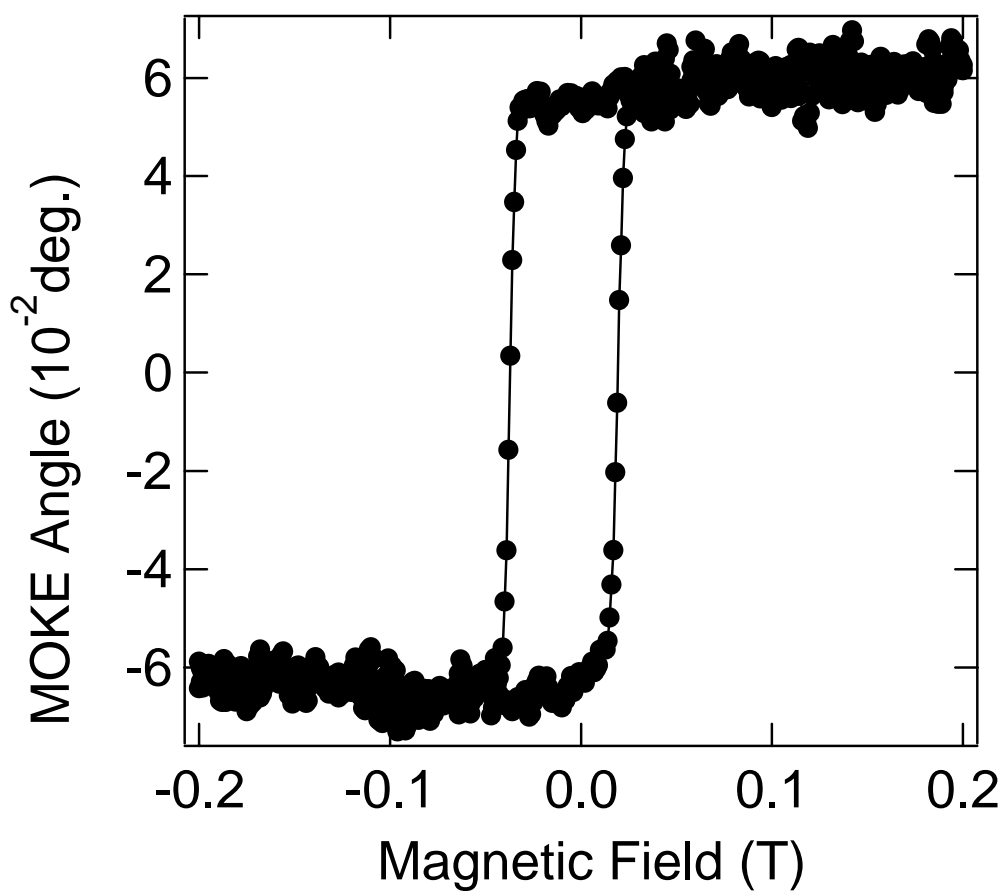


Fig. 34 MOKE signal vs. magnetic field for K22d. This data was taken at 30 K using the 780 nm laser diode. A Kerr rotation angle of 0.06 degree can be deduced here.

of the balanced detector. A MOKE rotation angle of 0.06 degrees of the sample at 30K and wavelength 780nm can be deduced from the vertical amplitude of the hysteresis loop, with our knowledge of the signal size when one of the detectors is blocked. This MOKE angle is the same order of the typical MOKE angle for InMnAs heterostructures observed in the previous study [26]. The coercive field for K285 at $T = 30$ K deduced from this CW-MOKE data (0.03 T) is similar to what we deduced from our CW-MCD measurements (Fig. 30).

Section 6-4 MOKE measurements with fs second laser pulses

In order to perform two-color time resolved measurements I described in previous chapter, static MOKE measurements with fs laser pulses are needed to be done. Shown in Fig. 31 is one example of CW MOKE data of sample K22d at 9.5K using a small fraction of energy in conjunction with a Gated Integrator and Boxcar Averager (SR250, Stanford Research System, Inc) and a New Focus pair detector as described previously.

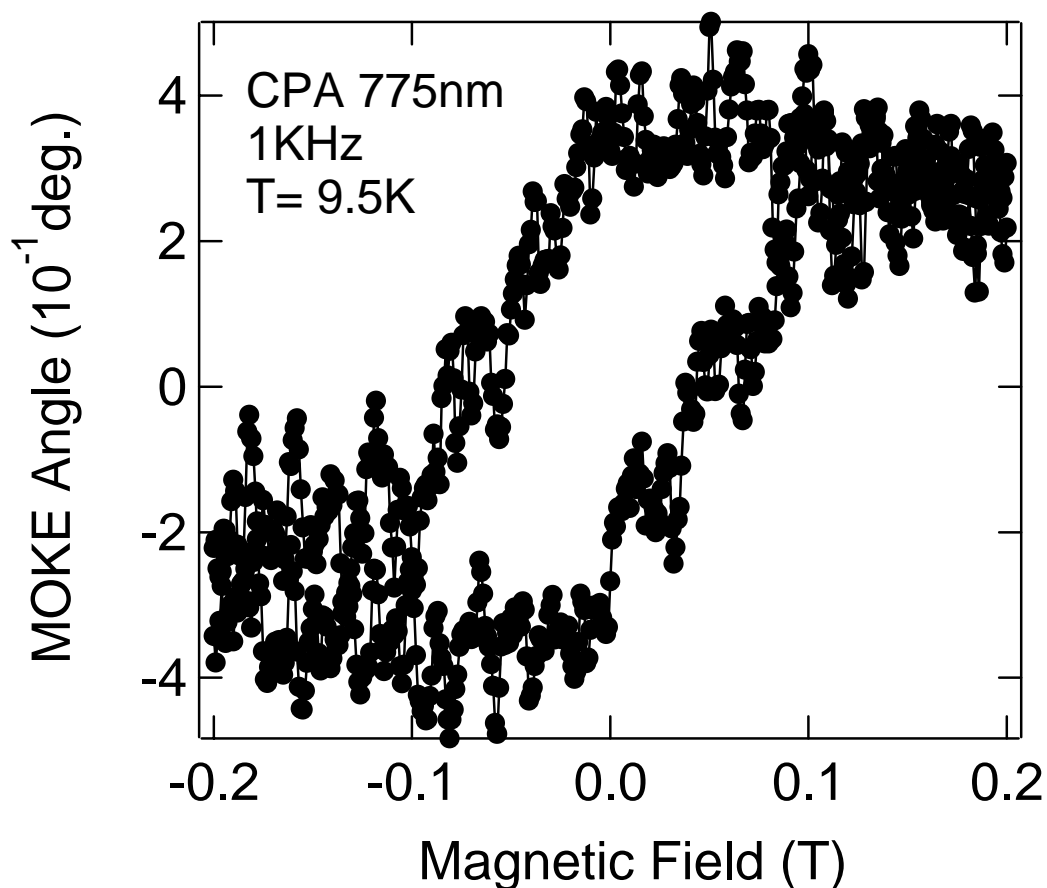


Fig. 35 MOKE signal vs. magnetic field for K22d. This data was taken at 9.5 using a CPA with wavelength 775nm, 1KHz repetition rate.

The gate width and the delay time of SR250 are chosen as 500ns and 760ns in the measurements in order to optimize the signal. And 1000 pulses are taken at one time and averaged for one data point. The regenerative frequency 1 KHz from CPA is used as external trigger input to the Gated Integrator and Boxcar Averager. Through this way we recover this small MOKE signal out of a large noise background (see Chapter 6, section 5 for the design idea of data acquisition). Hysteresis loop is clearly seen in Fig. 30. This clear demonstrates our current setup is sensitive enough to the magnetization change inside the sample. A MOKE rotation angle around 0.3 degrees at 9.5K and 775nm can be deduced from the vertical amplitude of the hysteresis loop, with our knowledge of the signal size when one of the detectors is blocked. Another feature of hysteresis loop here is the shape of the loop is tilted in comparison with the CW-MOKE/MCD measurements at high temperature (see Figs. 26). This feature is common in this system, which is also shown in the SQUID measurements. So it is not due to our fs laser light source. I will discuss this latter in section 7 in this chapter.

Section 6-4 Transit transmission measurements of GaAs

In order to test our optical setup of two-color time-resolved MOKE spectroscopy and determine the timing zero, two-color pump-probe measurements of test sample GaAs is made.

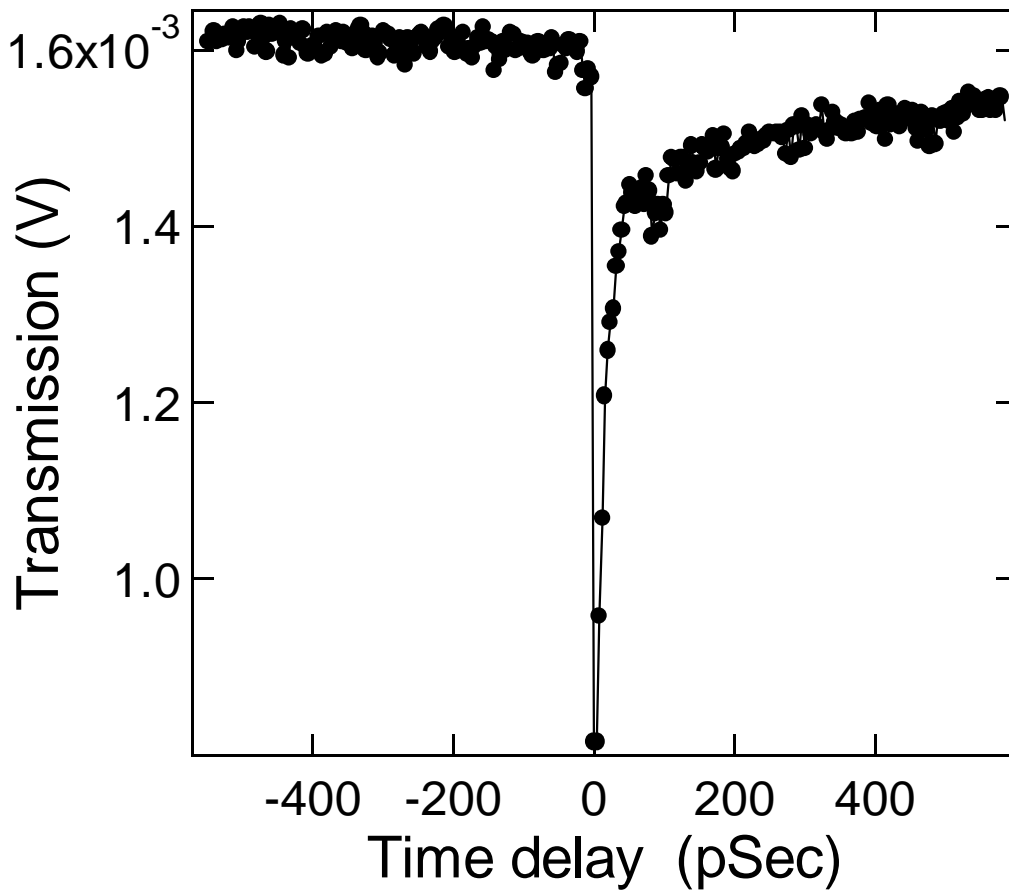


Fig. 36 Two-color time resolved pump-probe measurements of test sample GaAs. Pump light wavelength is 775 nm from CPA. Probe light wavelength is 2 μm from the idler output of OPA. The data was taken at room temperature.

Here, the transmission geometry is used. A 77K MCT detector (MCT20-010-E-LN4, Electro-Optical System, Inc) recorded the light intensity from idler output of OPA at 2 μm after it transmitted from the GaAs. 775 nm light from CPA light served as a pump light to create transit carriers in the conduction band. A clear photo-induced transit transmission change is observed. The key features of data here are the sharp decrease (within 1 picosecond) and slow recovery of transmission. The first feature is due to the instantaneous absorption of energy of a 2 μm probe pulse by the transit carriers created by a 150 fs pump pulse at the conduction band. We can define the timing zero at our setup from this information. The second feature is due to the long carrier relaxation time in bulk GaAs (around 1 ns).

Section 6-5 Two-color time-resolved MOKE

In the two-color time-resolved MOKE measurements, a CPA (775nm and 1 kHz repetition rate) and an OPA are used as pump and probe light source, respectively. 2 μm light from output of OPA idler mode with a pulse duration around 150 fs, photon energy 0.62 eV and fluence around 11.25 J/cm^2 is used to create transit carriers inside the magnetic layer InMnAs. The pump pulses beam diameter are focused onto the sample by

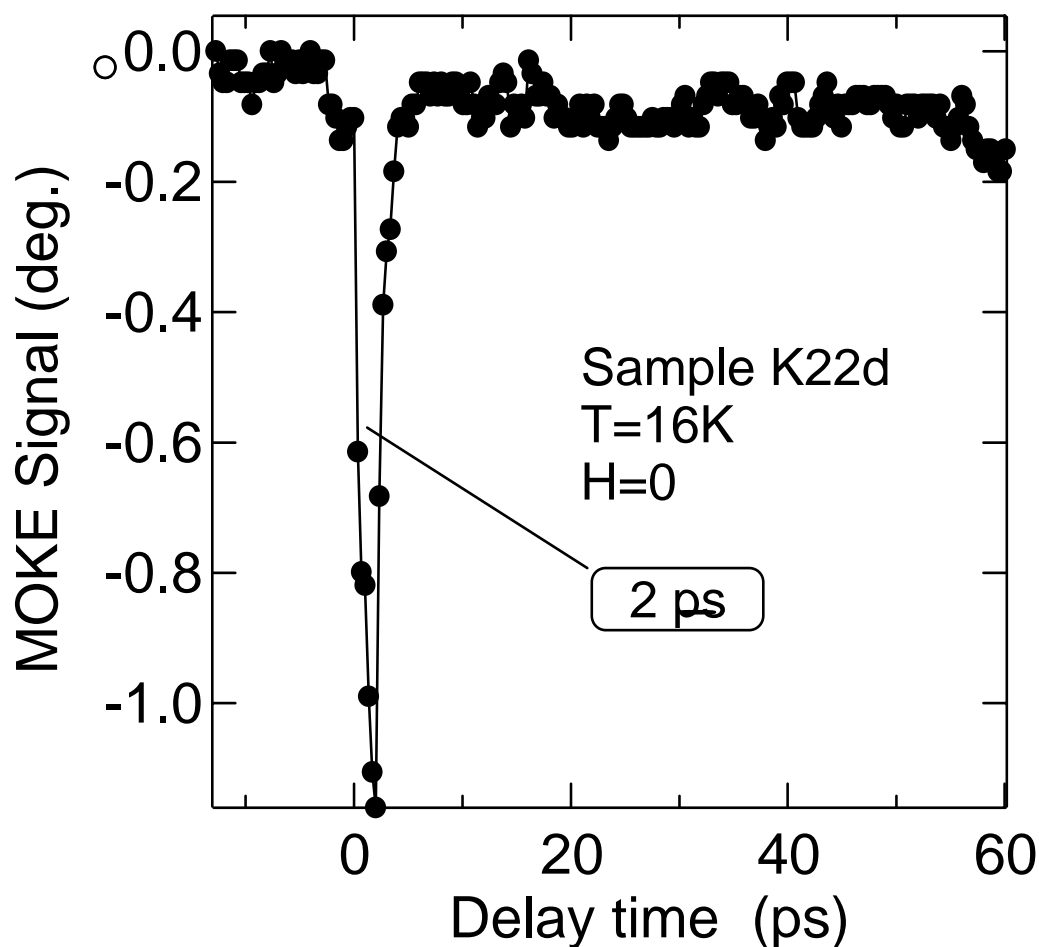


Fig. 37 Two-color time resolved MOKE measurements of K22d InMnAs heterostructure. Pump light with wavelength $2\mu\text{m}$ is from an OPA. Probe light with wavelength 775 nm is from a CPA. The data was taken at zero field and 16K. A 2 ps photo-induced MOKE response is clearly seen.

a parabolic mirror with 6 inch focal length. The time delay of the probe pulses from CPA is adjusted by a delay stage (Newport, Inc), which can be varied from several hundred *picoseconds*. The pump-probe MOKE measurements are also performed in polar Kerr configuration, and the polarization change of the signal is measured by a polarization balance bridge technique as described in the previous chapter. A Gated Integrator and Boxcar Averager record the signal. When the pump and probe pulse overlap spatially and temporally, an ultrafast photo-induced MOKE response is clear observed (Fig.37). The MOKE signal in the current case is proportional to $p*M$, where M is the magnetization of the sample under study and p is multiplication factor which is proportional to the reflective coefficient at the 775 nm probe frequency. So the transit MOKE signal in Fig. 30 should be interpreted as the ultrafast change of both reflection coefficient and the magnetization of the sample induced by transit carriers. Since the relative change of reflection coefficient ($\Delta R/R$) is proportional to the relative change of reflection intensity ($\Delta I_R/I_R$), we can get

$$\frac{\Delta\theta}{\theta} = \frac{\Delta I_R}{I_R} \pm \frac{\Delta M}{M}$$

Where M is the magnetization of the sample and +/- sign is determined by initial polarization of the CPA probe pulses before they hit the sample, which is set by a polarizer either 45 degree or 135 degree with respect to s or p direction. So if the first several *picoseconds* photo-induced response in Fig. 37 is totally dominated by the reflection change, we shouldn't expect any change of the sign of this ultrafast MOKE response when the input probe beam polarization changes from 45 degree to 135 degree. But it is not the case. Fig. 38 clearly shows the sign of photo-induced MOKE response

changes from negative to positive when the input beam polarization changes from 45 to 135 degree. So we can

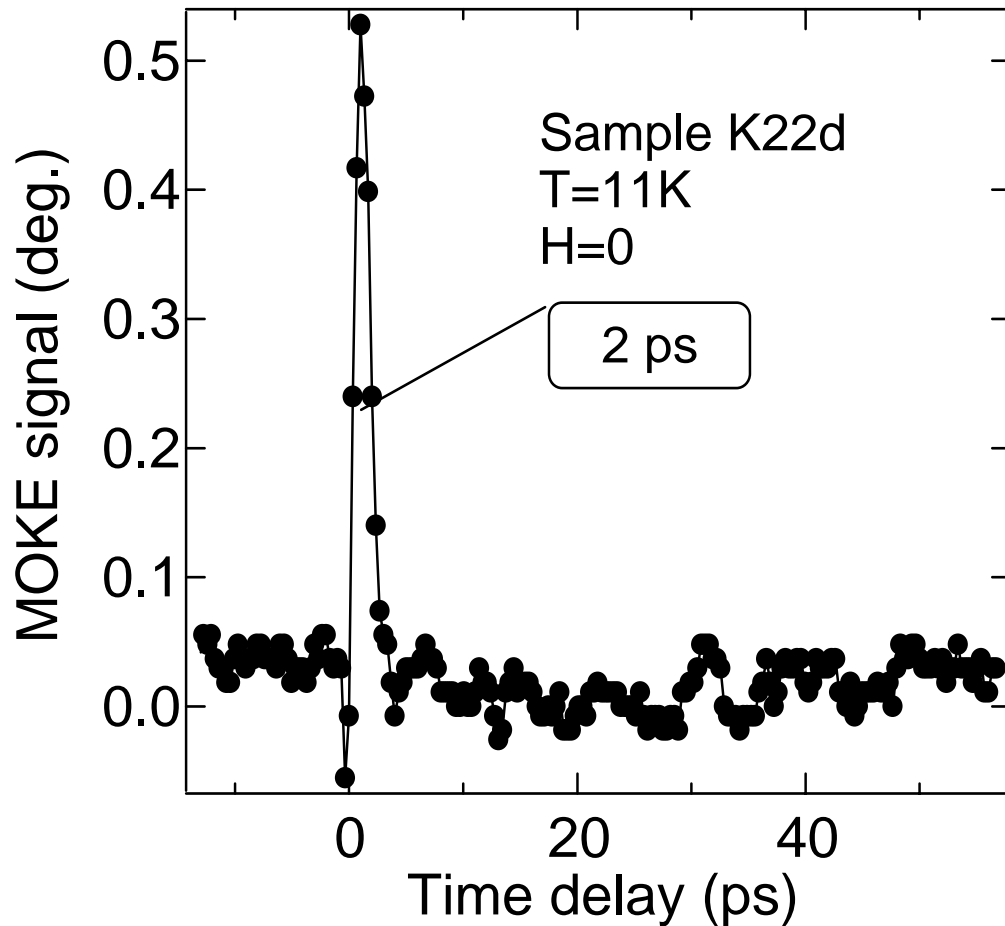


Fig. 38 Two-color time resolved MOKE measurements of K22d InMnAs heterostructure. Pump light with wavelength $2\mu\text{m}$ is from an OPA. Probe light with wavelength 775 nm is from a CPA. The data was taken at zero field and 16K. A 2 ps photo-induced MOKE response is clearly seen.

conclude the current ultrafast MOKE response should be a mixing effect of transit change of reflection and magnetization induced by photo-generated carriers.

Another key feature of this ultrafast photo-induced response is the very fast relaxation time (2 ps) in the MOKE signal in comparison with the carrier relaxation time in the normal narrow gap semiconductor (>1 ns, normally). In the current InMnAs/GaSb heterostructures, the carrier lifetime is expected to be short since this type of DMS structure is grown by low temperature MBE (Low-MBE) technique. Just like Low-MBE growth of GaAs used in the Auston switch to generate Terahertz pulse, the carrier relaxation process in this sample is expected to be very fast. However, We can't get the exact value of spin lifetime or carrier lifetime directly from current data since the current ultrafast MOKE response should be a mixing effect of transit change of reflection and magnetization. One should differentiate the carrier lifetime and spin lifetime when one interprets the current the data. The transit reflection change determines the carrier lifetime. The transit magnetization change determines the spin lifetime. These two time scales can be very different in the different materials and structure (for semiconductor case, see []; for ferromagnetic metal, see [], for half metallic ferromagnet, see []). But in ferromagnetic semiconductor, no result has been published to address this very important problem. Current study defiantly shine new light on this very important problem. However, since the current MOKE response is believed to be a mixing of carrier lifetime and spin lifetime, we need do more measurements to exact the exact value of spin /carrier. One of the most direct measurements to address this problem would be to record the transit reflection change as well as transit MOKE response at the same time.

Finally, I'd like to calculate how much transit carriers we can create inside the magnetic layers. The beam diameter of pump pulses after focusing is around 5 μm (r), which is measured by a set of pinholes. From the sample structure one can know the

thickness of magnetic layer is 25 nm (l_0). The other parameters used in my estimation are: energy per pulse $W = 8.8 \times 10^{-6}$ J; absorption coefficient $\alpha = 4.3 \times 10^3$ /cm.

$$n = W(1 - e^{-\alpha l_0}) / (\hbar \omega * S * l_0)$$

where $S = \pi r^2$. From above, one can get the transit holes $n = 0.79 * 10^{22}$ cm⁻³ is created inside magnetic layer in comparison with the original holes inside 1.1×10^{19} cm⁻³.

Section 6-6 measurements of non-equilibrium magnetic properties

From the estimation I made above, one can the photo-generated carriers will be around 3 times large the intrinsic carriers. Such large density of transit, photo-induced carriers within the InMnAs magnetic layer will strongly modify the various interactions inside the magnetic layer in an ultrafast manner. For instance, one should expect the p - d exchange coupling, which is crucial for the carrier-induced ferromagnetism in III-Mn-V system, will be *strongly and ultrafast* dressed. Equally, one should expect the ferromagnetism will also be *strongly and ultrafast* perturbed. And the ferromagnetic properties of this “non-equilibrium” ferromagnet should follow the same manner. One interesting possibility is to switch a semiconductor material between a “hard” ferromagnet and a “soft” ferromagnet in an ultrafast manner, for instance, in picosecond time scale, which are never seen in the semiconductor in any previous study. This new functionality will be expected to exert big impact to current information storage and processing technology [14].

The first measurements of non-equilibrium ferromagnetic properties of ferromagnetic semiconductor are shown in Fig. 39. At these measurements, the transit MOKE signals were recorded verses magnetic field at different time delay. In the upper panel, one example of magnetic field sweep at negative time delay (~ 7 ps) is plotted. Here pump pulse arrives after the probe pulse, thus should have no effect to the ferromagnetism of sample. In this case, the ferromagnetic hysteresis loop similar to the loop obtained from static MOKE measurements is seen. In the lower panel of Fig.39, the time delay was set to be 1 picosecond, which is around the peak of the ultrafast photo-

induced MOKE response (Fig.37). Comparing these two figures carefully, we can notice at least two new features induced by those transit carriers. First, the coercivity of the original ferromagnetic loop collapse. That means a “hard” ferromagnet is really converted into a “soft” ferromagnet in the picosecond time scale. The results here are consistent with previous CW experiment of the same material system, which is also a persistent photoconductivity effect and thus need a long build-up time (30 minutes halogen lamp illumination and 20 minutes waiting at dark) []. We can interpret current data in terms of *ultrafast, strongly optical dressed* domain wall energy due to the transit carriers. The domain wall energy, which determines the magnitude of coercivity field, includes three parts: exchange energy, anisotropy energy and a Zeeman energy term

$$E_i = K \sin^2 \theta_i - \sum J_{ij} S^2 \cos \phi_{ij} - SH \cos \theta_i$$

where K and J_{ij} is a magnetic anisotropy constant and exchange coupling constant, respectively. The exchange coupling will be enhanced due to the increase of carriers. Such *optical dressed* exchanged coupling leads to the increase of absolute value in the exchange energy term and thus reduces the total domain wall energy. The previous study of angular dependent magnetization measurements show the magnetic anisotropy energy K is not sensitive at all to the light illumination []. So overall effect of light illumination will reduce the total domain wall energy. This *Ultrafast, optical dressed* domain wall energy will get smaller, which means one need a smaller reverse magnetic field to flip the spin inside the ferromagnet.

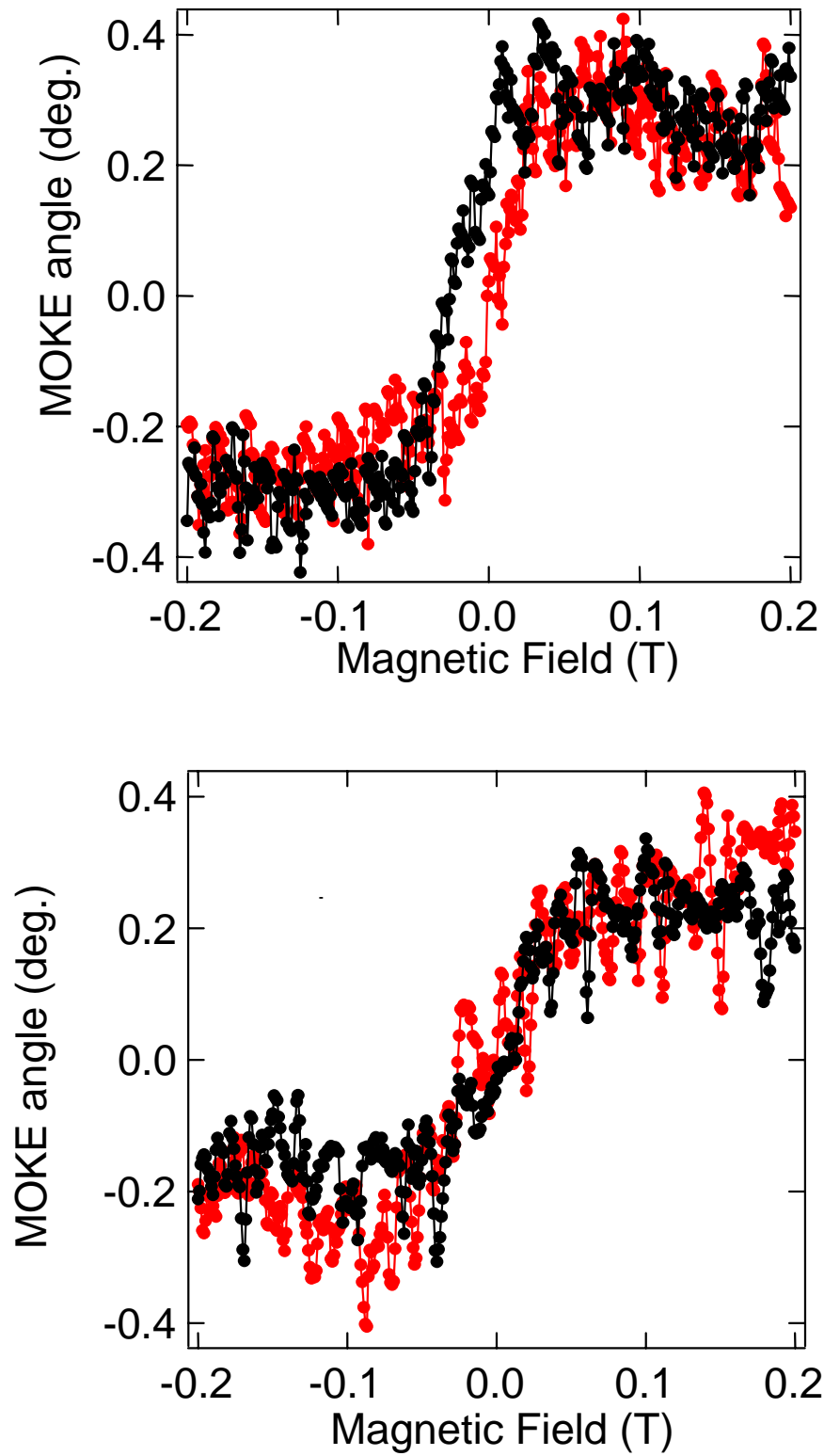


Fig. 39 Field sweeps at different time delay. Upper panel: $t < 0$; lower upper: $t \sim 1$ ps.

As stated above, photo-induced transit carriers are almost three magnitudes larger than the number of carriers originally existed in the sample. Transit carrier dynamics will totally dominate the response of domain wall energy at first several *picoseconds*. This ultrafast change of domain wall energy contributes to the ultrafast collapse of coercivity inside the ferromagnetic sample. The second feature seen from the data of non-equilibrium magnetic properties measurements is the ultrafast demagnetization at the first several *picoseconds*. From Fig.39 one can see the magnitude of the remnant magnetization is decreasing. The mechanism is not clear right now. More measurements are needed to interpret this phenomenon.

Section 6-7 Open questions

In the above sections, we discussed the various physics behind of our results of CW-MOKE/MCD and two-color time resolved MOKE. However, there are still some unsolved questions in the existing data or the physics unclear right now. These problems need to be identified and solved in the future work. These open questions include:

1. We see a large horizontal shift of the magnetic hysteresis, which is sample dependent. For K285, the horizontal shift is positive and for R1351 the horizontal shift is negative, but disappears for sample K22d.
2. The shape of hysteresis loop at high temperature is tilted comparing to high temperature data (see fig.). In order to highlight this point, Fig. 40 shows you the MCD data of sample K22d measured at 20 K and 10 K. Here the shape change of loop is clear. The possible reason can be the field sweep rate dependend of loop shape since the sweep rate of magnetic field can affect the final MCD/MOKE result if the magnetic heterostructures cannot respond quickly enough to the variation of the magnetic field. But this turns out not the case. Fig.41 shows you the magnetic sweep rate dependence of the MCD data. The MCD data was taken using the 780 nm laser diode. The difference in the hysteresis loop is not clear between the field sweeping rates of 0.05T/min or 0.15T/min. Our MOKE/MCD data are normally taken at the sweep rate between 0.05T/min or 0.15T/min. Besides, I need point out this feature of loop shape is also observed in the SQUID measurements. The physics behind it is not clear yet.

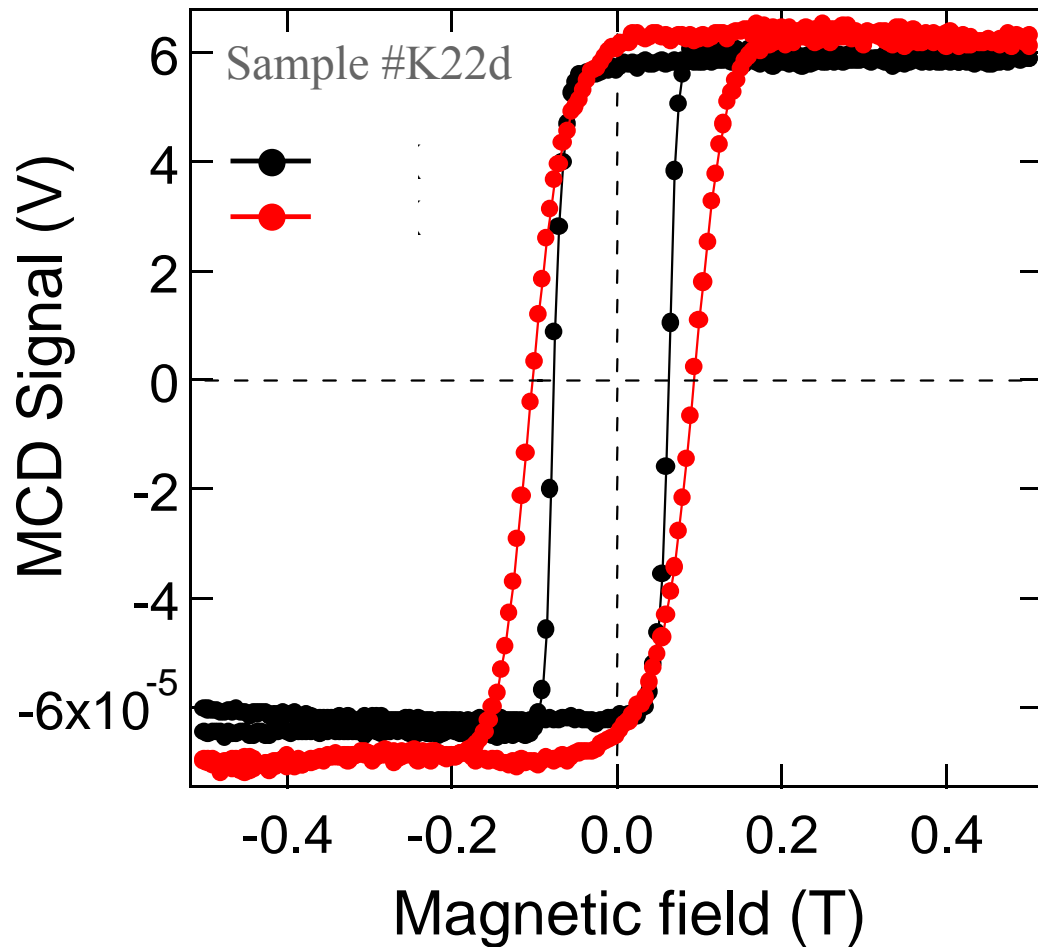


Fig. 40 Sweep range dependence of the horizontal offset of R1351. (780 nm probe light).

3. In the section 6-5, we discussed the results of the ultrafast photo-induced MOKE response (Fig. 37). But the story is not over yet. When I take more data points at the small time range focusing on the peak of this photo-induced MOKE signal, “double peak” appears inside the main structure (Fig. 42). The physics behind this fine structure is not clear yet. The possible reason includes existing the

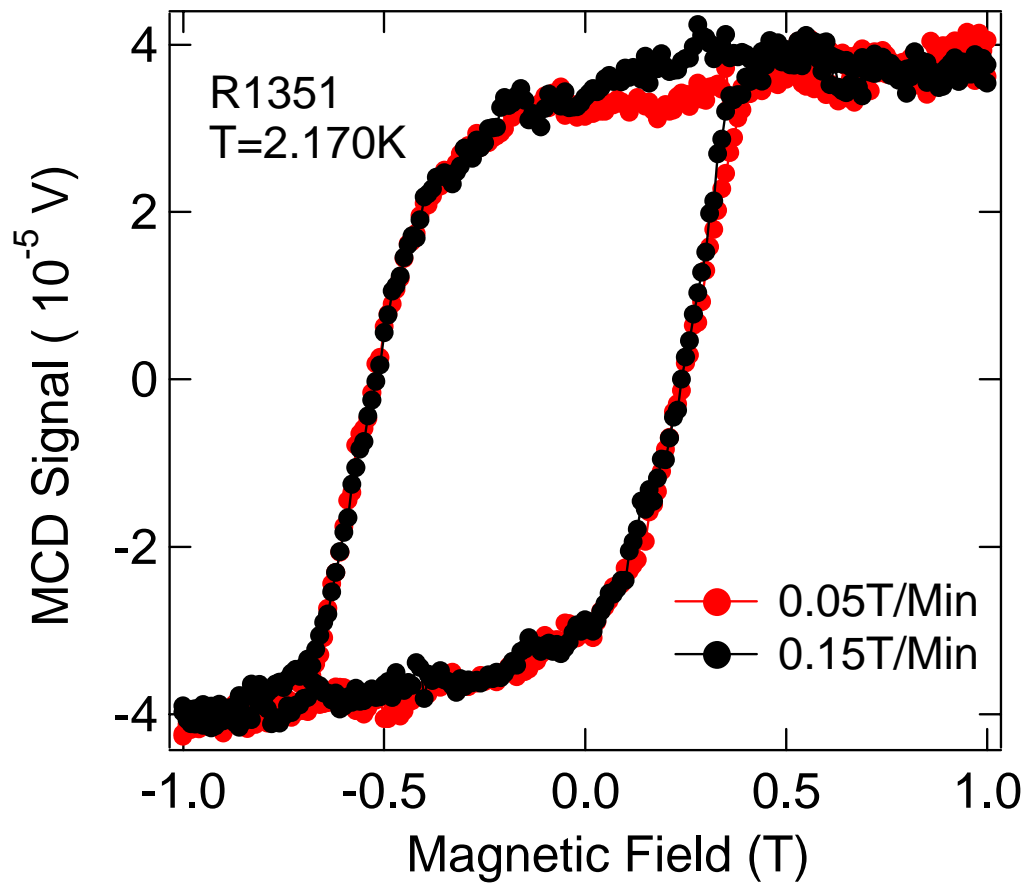


Fig. 41 Sweep rate dependence of the MCD curve for R1351 at $T = 2.170$ K. The two curves were taken with sweep rates of 0.15 Tesla/min and 0.05 Tesla/min.

pulse in the OPA pump pulse structure due the front and back reflection of some beam splitter inside the optical path.

4. The last issue is the ultrafast demagnetization observed in the measurements of non-equilibrium magnetic properties (Fig.39). More careful measurements and convincing data are needed to illustrate this phenomenon.

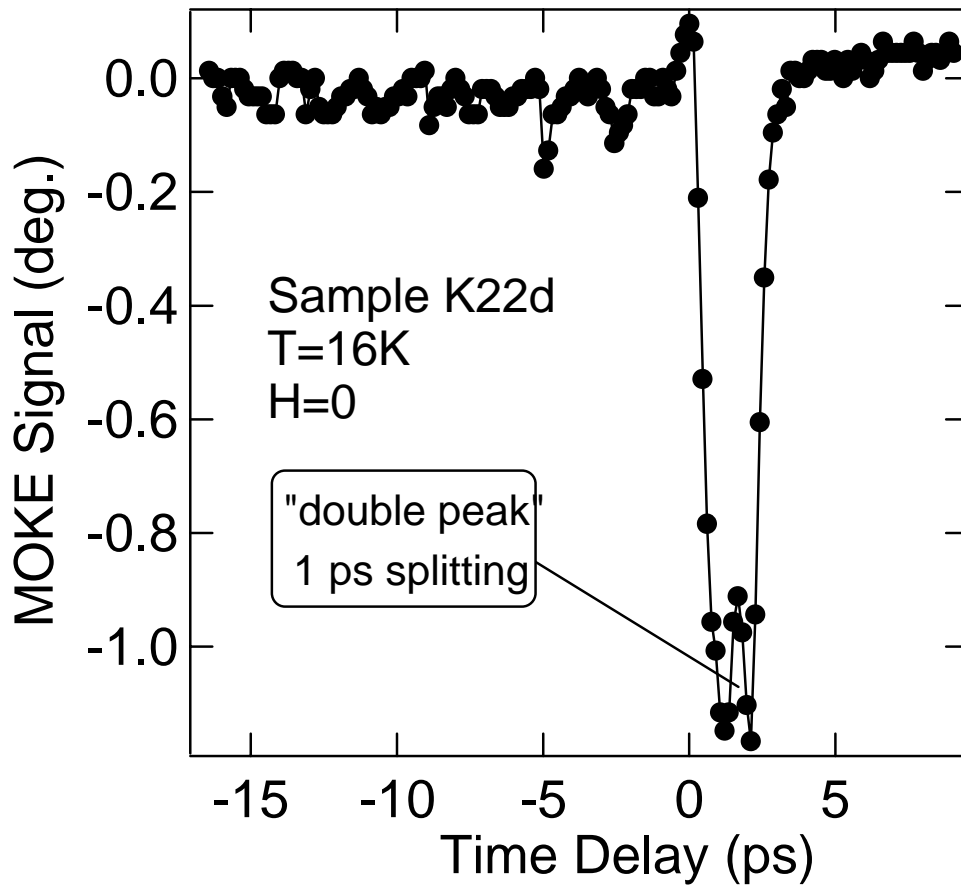


Fig. 42 Two-color time resolved MOKE measurements of K22d InMnAs heterostructure. Pump light with wavelength $2\mu\text{m}$ is from an OPA. Probe light with wavelength 775 nm is from a CPA. The data was taken at zero field and 16K . A 2 ps photo-induced MOKE response is clearly seen. "Double peak" appears inside the main structure.

